

On the Astrophysical Origin of Binary Black Hole Subpopulations: A Tale of Three Channels?

Anarya Ray ^{1,2,*}, Shirsha Mukherjee ^{3,†}, Michael Zevin ^{4,1,2} and Vicky Kalogera ^{1,2,5}

¹*Center for Interdisciplinary Exploration and Research in Astrophysics (CIERA),
Northwestern University, 1800 Sherman Ave, Evanston, IL 60201, USA*

²*NSF-Simons AI Institute for the Sky (SkAI), 172 E. Chestnut Street, Chicago, IL 60611, USA*

³*University of Oklahoma*

⁴*Adler Planetarium, 1300 South DuSable Lake Shore Drive, — Chicago, IL 60605*

⁵*Department of Physics and Astronomy, Northwestern University, 2145 Sheridan Road, Evanston, IL 60208, USA*

(Dated: March 19, 2026)

There is increasing evidence for multiple binary black hole (BBH) subpopulations in the cumulative gravitational wave catalog by the LIGO-Virgo-KAGRA Collaboration. The astrophysical interpretation of this complex underlying population is subject to theoretical uncertainties in treatments of binary stellar evolution, core collapse, and host environments. In this *Letter*, using parametrized mixture models, we show that the BBH detection sample comprises three astrophysical subpopulations that are likely dominated by specific formation channels. In particular, we show that the $10M_{\odot}$ peak and the $35M_{\odot}$ feature in the BBH mass spectrum correspond to distinct mass-ratio, spin alignment, spin precession, and redshift evolution properties. We show that mass-based transitions reported in the distribution of BBH parameters naturally emerge from our inferred distributions without explicit modeling. Our results are consistent with the current observed population arising from specific relative abundances of isolated binary evolution, dynamical formation in globular clusters, and higher-generation BBH mergers. Under this interpretation, we constrain the relative underlying fraction of these channels to be $79.0^{+11.5\%}_{-10.9\%}$, $14.5^{+11.6\%}_{-8.0\%}$, and $2.5^{+5.5\%}_{-1.8\%}$, respectively, and find these relative fractions to be evolving over cosmic time with more than 1σ confidence. Our interpretation relies on simple theoretical predictions that are mostly robust against uncertainties in BBH formation, with more definite conclusions expected in the near future.

Introduction — The fourth gravitational wave transient catalog [GWTC-4, 1] by LIGO-Virgo-KAGRA [LVK, 2–4] has revealed a complex underlying population of binary black hole (BBH) mergers [5]. With over 150 detections [1], there is increasing evidence of multiple subpopulations [6–13], indicating contributions from several formation channels [see, e.g. 14–16]. However, theoretical uncertainties in binary stellar evolution, BH formation through stellar collapse, and host environments often limit the scope of self-consistent astrophysical interpretation [see, e.g. 17, 18, for reviews]. Nevertheless, certain predictions remain robust against such uncertainties, which can be modeled in the growing population dataset to derive empirical constraints on key astrophysical parameters.

Broadly, theoretical models for BBH formation can be grouped into isolated binary evolution in galactic fields and dynamically interacting binaries in dense stellar environments, triple systems, or disks of active galactic nuclei [see, e.g., 17, 19, 20, for reviews]. Dynamical formation can be further categorized into first-generation “1G+1G” mergers that only comprise BHs formed directly through stellar collapse, and hierarchical mergers that comprise remnants of previous mergers retained by the environment [see, e.g., 21, for a review]. Despite the uncertainties in theoretical predictions, it is possible to disentangle these three subpopulations by modeling certain robust features that are largely independent of the underlying assumptions of binary stellar evolution, BH

formation, and treatment of host environments.

In particular, BHs formed directly through stellar collapse are expected to be slowly spinning at birth [22–24] as long as significant tidal interactions do not persist prior to core collapse [25–27] and exhibit a gap in the higher end of their mass-spectrum due to the pair instability process limiting the remnant mass or completely disrupting the high-mass progenitor in a pair instability supernova (PISN) [28–36]. On the other hand, remnants of previous mergers that retain a part of the original binary’s angular momentum prior to merger typically have high spin magnitude values of ~ 0.67 [37–41], and masses that can pollute the PISN gap [39, 42–48]. In addition, the strong recoil kicks received by merger remnants often lead to their expulsion from the dense environment [49–56]. Hence, the increasing rarity of higher-generation BHs that are available for forming binaries indicates a higher rate for hierarchical mergers between a second and a first generation companion (from here on 2G+1G) than all other combinations, leading to a strong preference for mass asymmetry in this subpopulation [39, 56–59].

Informed by these predictions, previous investigations that rely on semi-parametric mixture models have constrained the branching fraction of hierarchical mergers in the current observational sample, which is robust against the uncertainties in binary evolution and stellar collapse [8, 9, 11, 58–64]. From the maximum mass of the remaining ensemble, these studies have constrained the PISN cutoff and hence the carbon-oxygen reaction rate

in massive stars, a persistent theoretical uncertainty in the treatments of massive star evolution and the onset of the pair instability process. They have further provided a self-consistent astrophysical explanation for previously reported correlations in the BBH population, namely the broadening of the effective spin distribution with redshift and mass ratio, by showing that the highly-spinning, asymmetric-mass hierarchical subpopulation has a much steeper redshift evolution than the rest of the ensemble [8, 9].

However, there is additional substructure in the slowly spinning subpopulation whose interpretation requires further investigation [6, 10, 65–67]. This ensemble comprises $\sim 80\%$ of all astrophysical BBH mergers in the local universe [8, 9, 11, 60, 61] and exhibits two robust features in the mass spectrum near $10M_\odot$ and $35M_\odot$ [5]. Furthermore, it shows mass-based transitions in the distribution of BBH mass ratios and effective spins near $\sim 20M_\odot$ and $\sim 40M_\odot$ [6, 10]. Due to small spin magnitudes and preference for symmetric mass-ratio values, it is likely that this subpopulation comprises of systems where both components are first-generation BHs. In order to physically interpret the transition mass scales and isolate specific formation channels that might be responsible for various features in the mass distribution [68, 69], it is necessary to model distinct observational signatures of 1G+1G dynamical assembly and field evolution as BBH formation pathways that are also robust against persisting theoretical uncertainties.

Traditional dynamical assembly in dense stellar clusters is expected to result in isotropic spin orientations with respect to the orbit [70–72], although accretion from stellar mergers [73], evolution in gaseous environments [74–82], or hierarchical perturbers [83–85] may break this isotropy and lead to a higher propensity for aligned or in-plane spins. On the other hand, in isolated BBH formation, binary interactions such as mass transfer and tides are expected to preferentially align BH spin components to the orbital axis [86–89]. Hence, in the subpopulation of systems that do not comprise hierarchical mergers, it is possible to further disentangle the contributions of isolated binary evolution and various subchannels of 1G+1G dynamical mergers by modeling these potentially distinct spin properties. Note that these distinct trends in the distribution of component spins will also manifest in that of the effective aligned and effective precessing spin parameters of BBHs, which are often measured better than component spins for each individual detection.

In this *Letter*, we probe the astrophysical origins of the GWTC-4 detection sample and show that it can emerge from the mixing of three specific subpopulations that are consistent with the expectations of distinct formation channels. Using parametrized mixture models, we constrain the relative abundance of each subpopulation and how they evolve over cosmic time. We provide a

physical interpretation of mass-based transition scales reported in GWTC-4 that naturally emerge in our inferred distributions without explicit modeling. We identify new correlations between masses, redshifts, and effective precessing spins, and show that the two robust features in the mass spectrum likely arise from distinct formation channels. Our findings hint towards a self-consistent interpretation of the current observed population as emerging from specific relative abundances of isolated binary evolution, 1G+1G dynamical formation, and hierarchical mergers, with relative contributions that vary across cosmic time.

Methods — We investigate the hypothesis that subpopulations originating from specific formation channels give rise to particular features in the mass spectrum, whose combined contributions can self-consistently explain the mass-based transitions observed in the distributions of other BBH parameters. To that end, we model the population-level distribution of BBH primary masses (m_1), mass ratios (q), effective aligned spins (χ_{eff}), effective precessing spins (χ_p), and redshifts (z), as a three-component mixture. Each component is constructed from simple parametrizations that are motivated by the findings of data-driven studies and are capable of capturing specific features in the mass spectrum that have been robustly identified by past investigations [5, 6, 10]. We delineate these parametrizations in Table I. Note that we target the hierarchical sub-

Comp.	$p(m_1)$	$p(q m_1)$	$p(\chi_{eff})$	$p(\chi_p)$	$r(z)$
1	PLP	$\mathcal{N}_{[\frac{m_2, min}{m_1}, 1]}^{\mu_q^1, \sigma_q^1}$	$\mathcal{N}_{[-1, 1]}^{\mu_{\chi_{eff}}^1, \sigma_{\chi_{eff}}^1}$	$\mathcal{N}_{[0, 1]}^{\mu_{\chi_p}^1, \sigma_{\chi_p}^1}$	$(1+z)^{\kappa_1}$
2	BPL	$\text{SPL}_{[\frac{m_2, min}{m_1}, 1]}^{\beta_q, \frac{\delta m}{m_1}}$	$\mathcal{N}_{[-1, 1]}^{\mu_{\chi_{eff}}^2, \sigma_{\chi_{eff}}^2}$	$\mathcal{N}_{[0, 1]}^{\mu_{\chi_p}^2, \sigma_{\chi_p}^2}$	$(1+z)^{\kappa_2}$
3	BPL	$\mathcal{N}_{[\frac{m_2, min}{m_1}, 1]}^{0.5, \sigma_q^3}$	$\mathcal{U}(-w, w)$	$\mathcal{N}_{[0, 1]}^{\mu_{\chi_p}^3, \sigma_{\chi_p}^3}$	$(1+z)^{\kappa_3}$

TABLE I. Parametrizations of each component. Here $\text{SPL}_{a,b}^{\beta,\delta}$ denotes a single smoothed powerlaw with index β , and smoothing parameter δ , truncated within $[a, b]$, PLP denotes a smoothed Powerlaw+Gaussian Peak, BPL a smoothed broken powerlaw, $\mathcal{N}_{[a,b]}^{\mu,\sigma}$ a Gaussian with mean μ , and variance σ^2 truncated within $[a, b]$, and $r(z)$ is the ratio of the merger rate at redshift z relative to the local rate (i.e. at $z = 0$).

population with component 3 but do not enforce its existence [8, 9, 60], while allowing much higher flexibility through the parametrizations of the other two components. We explore variations in modeling assumptions by considering alternative functional forms and by relaxing prior restrictions, and find that our results are robust against such variations. Detailed functional forms of our models, the corresponding hyperpriors, model comparison tests, and additional checks for model systematics are presented as supplemental material.

In a mixture of subpopulations with potentially distinct q , χ_{eff} , χ_p , z distributions, one can expect the emer-

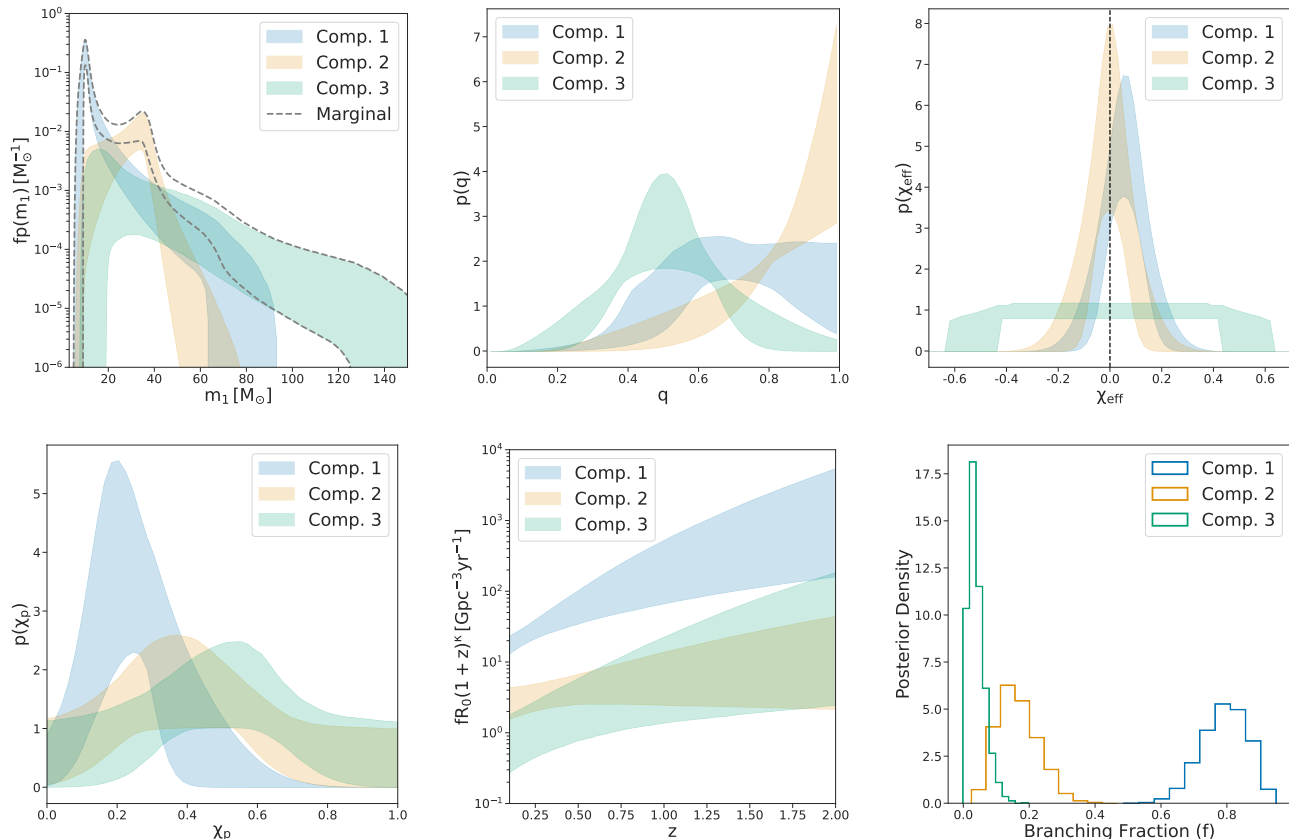


FIG. 1. Distributions of primary mass (weighted by the branching fractions, *top left*), mass-ratio (*top center*), effective aligned (*top right*) and precessing (*bottom left*) spins for each component. The redshift evolution of the merger rate (*bottom center*) and branching fractions (*bottom right*) are also shown. See supplemental material for comparisons with prior-predictive draws.

gence of several mass scales that demarcate transitions in the marginal distributions of these BBH parameters. Such transition scales can distinguish the mass ranges in which different formation channels contribute dominantly to the astrophysical merger rate. We define m_t^{12} such that for $m_1 \leq m_t^{12}$, the contribution from component 1 dominates that of the others. Similarly m_t^{23} is defined such that for $m_t^{12} \leq m_1 \leq m_t^{23}$, component 2 has the highest relative abundance. We reconstruct these numbers from the inferred distributions in postprocessing¹, since these are not hyperparameters that constrain our distribution functions.

Results — We constrain our mixture model from GWTC-4 data publicly released by the LVK [90–96], using a Bayesian hierarchical analysis [19, 97–102], and reconstruct the $m_1, q, \chi_{eff}, \chi_p, z$ distributions of each component. From the inferred distributions, we compute the

emergent transition mass scales. Our model is preferred by the data over a single-component default distribution that comprises a broken power law plus two peaks in m_1 [5], single powerlaws in q and z , and single truncated Gaussians for χ_{eff} and χ_p , by a Bayes factor of 10^6 .

In Figure 1, we show the inferred distributions of BBH parameters for each mixture component. There is evidence of three distinct subpopulations, whose unique features in the distributions of intrinsic BBH parameters are presented as follows.

1. *Subpopulation 1 (Comp. 1)*: This component peaks sharply at $10M_\odot$ and falls off like a powerlaw up to a maximum mass of $70.0^{+21.7}_{-7.5}M_\odot$. The χ_{eff} distribution narrowly peaks at a small but positive value, with $23.0^{+12.9}_{-10.3}\%$ systems having $\chi_{eff} < 0$, demonstrating a preference for slowly spinning aligned systems. The mass ratio distribution appears flat in the 0.6–1.0 range, with hints of an over-density near 0.7 and a sharp falloff for smaller values. The χ_p spin distribution favours significantly smaller values than the other two subpopulations, indicating very few systems with in-plane spin components. These systems comprise $79.0^{+11.5}_{-10.9}\%$ of all astro-

¹ For each hyperparameter, the minimum m_1 on a grid above which $f_2 p_2(m_1) > f_1 p_1(m_1)$ is defined as m_t^{12} and the maximum m_1 below which $f_2 p_2(m_1) \geq \max\{f_1 p_1(m_1), f_3 p_3(m_1)\}$ is defined as m_t^{23}

Comp.	$m_1 \leq m_t^{12}$	$m_t^{12} \leq m_1 \leq m_t^{23}$	$m_t^{23} \leq m_1 \leq m_{max,(1or2)}$	$m_1 > m_{max,(1or2)}$
1	$96.3^{+1.8}_{-5.0}\%$	$16.3^{+11.9}_{-8.3}\%$	$45.4^{+26.9}_{-37.7}\%$	0.0%
2	$2.5^{+4.0}_{-1.2}\%$	$74.6^{+10.8}_{-14.0}\%$	$9.1^{+10.1}_{-4.3}\%$	0.0%
3	$0.34^{+3.67}_{-0.34}\%$	$5.8^{+11.6}_{-4.8}\%$	$51.6^{+29.0}_{-37.1}\%$	100%

TABLE II. Relative abundance of various components in different mass ranges.

physical BBH mergers in the local universe.

- Subpopulation 2 (Comp. 2)*: This subpopulation displays a very shallow rise in the mass spectrum with no sharp feature near $10M_\odot$ but clearly captures the $35M_\odot$ peak. At higher masses, the merger rate for this component falls off much more sharply than that of Subpopulation 1, until a similar maximum mass. The mass-ratio distribution peaks strongly at $q = 1$, demonstrating a strong preference for equal-mass binaries. The χ_{eff} values of these systems are narrowly concentrated about zero, with $51.7^{+16.1}_{-17.1}\%$ systems having $\chi_{eff} < 0$, indicating small spin magnitudes and equal fractions of aligned and antialigned spin orientations with respect to the orbit. The χ_p distribution peaks at significantly higher values than Subpopulation 1, demonstrating a higher fraction of systems with in-plane spin components. This equal mass, slowly spinning subpopulation with isotropically oriented spin components and an overabundance of systems in $30 - 40M_\odot$ contributes $14.5^{+11.6}_{-8.0}\%$ of all local BBHs.
- Subpopulation 3 (Comp. 3)*: This component shows a shallow decline in the mass spectrum spanning from $12.7^{+5.1}_{-6.5}M_\odot - 140.0^{+43.4}_{-15.0}M_\odot$, a mass-ratio distribution strongly preferring values smaller than $q = 0.7$, a broad and relatively flat effective spin distribution between -0.5 and 0.5 , and marginally higher precession than component 2. The break in the powerlaw of this component ($58.6^{+15.8}_{-24.3}M_\odot$) is inferred to be roughly twice the break mass of component 2 ($36.1^{+2.1}_{-2.5}M_\odot$). This subpopulation contributes to $2.5^{+5.5}_{-1.8}\%$ of merging BBHs in the local universe.

We find that component 2, i.e., the one responsible for the $35M_\odot$ peak, has a much shallower redshift evolution ($\kappa_2 = 1.59^{+1.61}_{-1.84}$) than the other two, whereas components 1 and 3 have redshift evolutions with similar slope ($\kappa_1 = 3.89^{+2.03}_{-1.61}$, $\kappa_3 = 3.75^{+2.01}_{-2.34}$). Even though these 90% bounds of κ_i overlap, the 1σ intervals do not, indicating a redshift evolving mass spectrum at more than 68% confidence (see supplemental material).

As evident from the weighted mass spectra of the different components, the GWTC-4 detection sample indicates that there are two mass scales at which the q , χ_{eff} , χ_p , and z distributions transition into different shapes. We constrain these transition scales from our

inferred mass distributions and branching fractions to be $m_t^{12} = 23.3^{+4.2}_{-7.0}M_\odot$, and $m_t^{23} = 41.8^{+5.4}_{-4.3}M_\odot$. These are fully consistent with previous investigations that have directly modelled mass-based transitions in the distribution of these parameters [6, 7, 62, 63, 103]. We constrain the relative abundance of our three channel-specific subpopulations in each region spanned by the transition masses in Table II. We compare the marginal distributions of these BBH parameters above and below the transition masses with the previous findings of data-driven analyses [10] in the supplemental materials. Note that in particular, the region $m_t^{23} \leq m_1 \leq m_{max}^1$ has comparable contributions from *Comp. 1* and *Comp. 3*. This leads to a marginal mass-ratio distribution in that region which has a much higher fraction of events with $q > 0.7$ than expected from *Comp. 3* alone [7].

Astrophysical Interpretation — Our results reveal new correlations in the BBH populations (such as the distinct redshift evolution and spin precession properties of the $10M_\odot$ and $35M_\odot$ subpopulations) and provide a self-consistent interpretation of previously reported ones. In particular, mass-based transitions in the distributions of BBH parameters naturally emerge in our inferred distributions without explicit modeling. We have performed rigorous model selection studies and compared our results with those of data-driven analyses to show (in the supplemental material, Tables I, VII, Figure 8) that our findings are not driven by prior assumptions. We now discuss the astrophysical interpretation of these features being present in the data, which is largely independent of theoretical uncertainties in binary stellar evolution, BH formation, and properties of host environments.

To that end, we start by quantifying robust tracers of BBH evolutionary pathways from our inferred distributions [104, 105], namely, the fraction of $\chi_{eff} < 0$ events ($P(\chi_{eff} < 0)$), the width of the χ_{eff} distribution ($\sigma_{\chi_{eff}}$), the median of the χ_p distributions ($\bar{\chi}_p$), and the fraction of $q > 0.7$ events ($P(q > 0.7)$), for each subpopulation, which are presented in Table III. These metrics increase monotonically with astrophysically crucial properties. In particular, $P(\chi_{eff} < 0)$ increases monotonically with the fraction of anti-aligned systems, $\sigma_{\chi_{eff}}$ with typical spin magnitudes, ($\bar{\chi}_p$) with the preference for in-plane spin orientations, and $P(q > 0.7)$ with the preference for mass-symmetry. We now turn to predictions of BBH formation for these metrics that are largely independent of persisting theoretical uncertainties.

In isolated binary evolution, binary interactions such

Metric	Comp. 1	Comp. 2	Comp. 3
$P(\chi_{eff} < 0)$	$23.0^{+12.9}_{-10.3}\%$	$51.7^{+16.1}_{-17.1}\%$	$50^{+0}_{-0}\%$
$\sigma_{\chi_{eff}}$	$0.07^{+0.03}_{-0.02}$	$0.08^{+0.03}_{-0.03}$	$0.30^{+0.06}_{-0.05}$
$\bar{\chi}_p$	$0.24^{+0.07}_{-0.06}$	$0.49^{+0.05}_{-0.16}$	$0.50^{+0.10}_{-0.13}$
$P(q > 0.7)$	$50.52^{+20.32}_{-12.20}\%$	$83.64^{+10.01}_{-15.90}\%$	$11.00^{+9.98}_{-8.86}\%$

TABLE III. Metrics for astrophysical interpretation. For robustness against variation with functional forms and hyper-priors see supplemental material (Figures 4, 3).

as mass transfer and tides are expected to preferentially align spin orientations with the orbit [86–89]. Higher fractions of anti-aligned systems are only possible through large natal kicks imparted by the supernovae during BH formation [106–108]. However, large kick magnitudes can lead to disruption of the binary and are found to be inconsistent with observations of Galactic BH binary systems [109, 110]. Hence, for a subpopulation of isolated binaries, large values of $\bar{\chi}_p$, and $P(\chi_{eff} < 0) \sim 50\%$ are unlikely. This prediction is largely insensitive to uncertainties in binary evolution and stellar collapse except possibly for the potential of off-axis kicks that can toss the BH spin axis [111].

On the other hand, as BHs born through stellar collapse, the components of isolated binaries should either exhibit an upper mass gap due to the pair instability process or pollute it through mechanisms (such as super-Eddington accretion during mass-transfer onto the first-born BH or chemical mixing in tight binaries) that also lead to preferentially high spins and aligned spin orientations [34, 112, 113]. Very high mass, isotropic spin ($P(\chi_{eff} < 0) = 50\%$) systems are, therefore, also difficult to explain through the isolated channel.

For 1G+1G dynamical assembly in dense star clusters, randomization of spin orientations leads to equal preference for aligned and anti-aligned components [70–72]. Proposed methods for efficient spin alignment, such as BBH–star collisions [73], only comprise at most 10% of all cluster mergers and can also lead to high spin magnitudes [114], even though the latter is subject to uncertainties in accretion efficiency. This likely makes dynamical assembly inconsistent with subpopulations that simultaneously have small $\sigma_{\chi_{eff}}$, $P(\chi_{eff} < 0) \ll 50\%$, and large $\bar{\chi}_p$. This channel also prefers equal-mass binaries due to mass segregation causing heavier objects to sink to the center of the cluster [115–117], and strong gravitational interactions between three or more bodies preferentially leading to the more massive components forming a bound binary and ejecting less massive components [118]. While mechanisms for polluting the PISN gap through this channel have been proposed, the resulting mergers continue to prefer equal-mass systems [73, 114], leading to inconsistency with a high-mass subpopulation that exhibits strong mass asymmetry.

Similarly, BBH mergers with spins aligned to the orbit are unlikely to occur in triple systems, since Lidov–

Kozai resonance in the inner binary induced by a distant tertiary component can preferentially orient binary spins perpendicular to the orbit. The predicted distributions of cosine tilts are symmetric about a peak at zero [83–85, 119] which is consistent with high $\bar{\chi}_p$ and $P(\chi_{eff} < 0) \sim 50\%$, and inconsistent with both low $\bar{\chi}_p$ and $P(\chi_{eff} < 0) \ll 50\%$.

Finally, in the hierarchical channel, components that are remnants of previous mergers, through a robust prediction of numerical relativity simulations, have high spin magnitudes of ~ 0.67 , with dispersion dependent on spin magnitudes, orientations, and mass ratios [37–41]. This will lead to inconsistency with subpopulations that have small $\sigma_{\chi_{eff}}$. Furthermore, due to high recoil kicks, the rarity of retained merger remnants in dynamical environments leads to hierarchical mergers being predominantly 2G+1G systems which exhibit strong mass asymmetry, with less than a few percent of systems expected in the $q > 0.7$ range [49–56]. This channel can also straightforwardly pollute the PISN gap in m_1 , extending up to very high masses [39, 42–48].

Given these predictions that are largely robust against uncertainties in binary stellar evolution, BH formation, and properties of host environments, and the trends in our subpopulations summarized in Table III, we conclude that only specific channels likely contribute dominantly to each subpopulation, which is presented in Table IV.

Channel	Comp. 1	Comp. 2	Comp. 3
Isolated binaries	✓	✗	✗
1G+1G in clusters	✗	✓	✗
Triple systems	✗	✓	✗
Hierarchical	✗	✗	✓

TABLE IV. Plausible origins of each subpopulation. Here, ✓ means plausible and ✗ implies unlikely, that the corresponding channel contributes dominantly to the respective subpopulation.

While these conclusions are reasonably robust, the direct association of subpopulations with single channels remains elusive. In particular, dynamical formation in AGN disks can give rise to aligned, isotropic, and in-plane spin orientations depending on assumptions in the modeling of disk physics [74–82]. Similarly, this channel is capable of producing both equal and unequal mass systems depending on various underlying assumptions. In other words, this channel can, in principle, give rise to features consistent with all three subpopulations. On the other hand, for Subpopulation 2, it is unclear whether there is an excess of in-plane systems compared to what is expected for an isotropic distribution. While the χ_{eff} , and χ_p distributions can together elucidate this mystery, measurement uncertainties in GWTC-4 cannot distinguish between triples and dynamical assembly in dense star clusters as the origin of this subpopulation.

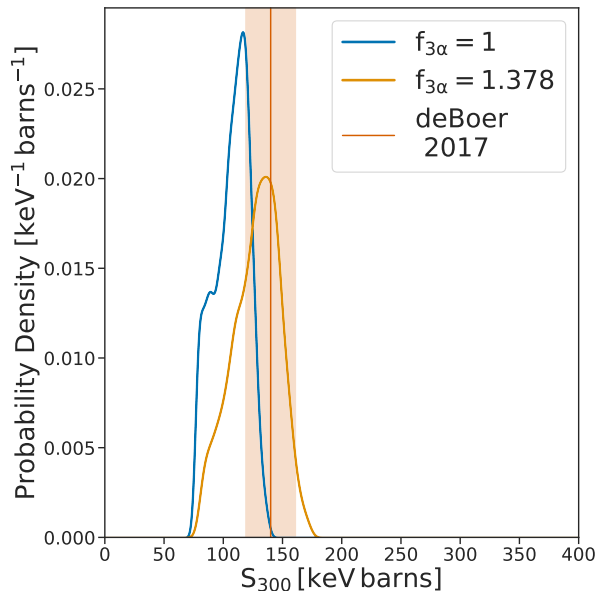


FIG. 2. Constraints on the S factor of $^{12}\text{C}(\alpha, \gamma)^{16}\text{O}$ at 300 keV obtained using the stellar models of Ref. [120], depending on the chosen rate of the 3α process, which were taken to be either equal to or 37.8% larger than the values reported in the NCARE compilation [120, 121].

Despite these degeneracies in interpretation, one possibility consistent with our observed subpopulations merits further discussion. Theoretical simulations show that isolated binary evolution through stable mass transfer can give rise to the $10M_{\odot}$ peak [122], support for mass ratios in the region 0.6–1.0 [27, 34, 123, 124], and a preference for slowly spinning components aligned to the orbits (as exhibited by Subpopulation 1). A sharp peak near $10M_{\odot}$ has not been predicted through AGN disks in existing literature to the best of our knowledge. Similarly, while both triples and 1G+1G mergers in star clusters can be consistent with the spin and mass ratio properties of Subpopulation 2, simulations of dynamical assembly in globular clusters have demonstrated an overdensity consistent with the $35M_{\odot}$ feature [125], whereas such predictions are yet to be made for triples. Furthermore, the ratio of branching fractions between Subpopulations 3 and 2 is $0.15^{+0.41}_{-0.11}$, which is consistent with theoretical expectations for the relative abundance of hierarchical and 1G+1G mergers in globular clusters [39]. Note, however, that the shallower redshift evolution of Subpopulation 2 relative to 3 would then imply a cluster mass function that likely evolves with redshift [8, 126, 127].

To summarize, we find that the GWTC-4 BBH sample of detections comprises three distinct subpopulations with local merger rates of $11.3^{+5.3}_{-4.0}\text{Gpc}^{-3}\text{yr}^{-1}$, $2.2^{+1.8}_{-1.1}\text{Gpc}^{-3}\text{yr}^{-1}$, and $0.42^{+0.76}_{-0.32}\text{Gpc}^{-3}\text{yr}^{-1}$, that are likely consistent with specific formation channels. Our

narrative interprets the mass-based transitions as emerging from the specific relative abundances of these three channels. Under this hypothesis, we interpret the common maximum mass of Subpopulations 1 (likely mergers from isolated binary evolution) and 2 (likely 1G+1G mergers in globular clusters) as the PISN cutoff and constrain the S factor of $^{12}\text{C}(\alpha, \gamma)^{16}\text{O}$ at 300 keV (Figure 2) to be in strong agreement with independent measurements [128]. With new data releases imminent by the LVK, and ongoing developments in detailed binary evolution modeling, robust conclusions on this hypothesis and more precise measurements of stellar-evolution uncertainties can be expected in the near future.

Acknowledgements — A.R. was supported by the National Science Foundation (NSF) award PHY-2512923. M.Z. gratefully acknowledges funding from the Brinson Foundation in support of astrophysics research at the Adler Planetarium. V.K. was supported by the Gordon and Betty Moore Foundation (grant awards GBMF8477 and GBMF12341), through a Guggenheim Fellowship, and the D. I. Linzer Distinguished University Professorship fund. We are grateful for the computational resources provided by the LIGO laboratory and supported by National Science Foundation Grants PHY-0757058 and PHY-0823459. This material is based upon work supported by NSF’s LIGO Laboratory, which is a major facility fully funded by the National Science Foundation. We gratefully acknowledge the support of the NSF-Simons AI-Institute for the Sky (SkAI) via grants NSF AST-2421845 and Simons Foundation MPS-AI-00010513.

* anarya.ray@northwestern.edu

† shirsha.mukherjee@ou.edu

- [1] A. G. Abac *et al.* (LIGO Scientific, VIRGO, KAGRA), GWTC-4.0: Updating the Gravitational-Wave Transient Catalog with Observations from the First Part of the Fourth LIGO-Virgo-KAGRA Observing Run, (2025), arXiv:2508.18082 [gr-qc].
- [2] J. Aasi *et al.* (LIGO Scientific), Advanced LIGO, *Class. Quant. Grav.* **32**, 074001 (2015), arXiv:1411.4547 [gr-qc].
- [3] F. Acernese *et al.* (Virgo), Advanced Virgo: a second-generation interferometric gravitational wave detector, *Class. Quant. Grav.* **32**, 024001 (2015), arXiv:1408.3978 [gr-qc].
- [4] T. Akutsu *et al.* (KAGRA), Overview of KAGRA: Calibration, detector characterization, physical environmental monitors, and the geophysics interferometer, *PTEP* **2021**, 05A102 (2021), arXiv:2009.09305 [gr-qc].
- [5] A. G. Abac *et al.* (LIGO Scientific, VIRGO, KAGRA), GWTC-4.0: Population Properties of Merging Compact Binaries, (2025), arXiv:2508.18083 [astro-ph.HE].
- [6] S. Banagiri, E. Thrane, and P. D. Lasky, Evidence for Three Subpopulations of Merging Binary Black Holes at Different Primary Masses, (2025), arXiv:2509.15646

- [astro-ph.HE].
- [7] A. Ray and V. Kalogera, Reexamining Evidence of a Pair-instability Mass Gap in the Binary Black Hole Population, *Astrophys. J. Lett.* **998**, L20 (2026), arXiv:2510.18867 [astro-ph.HE].
- [8] A. M. Farah, A. Vijaykumar, and M. Fishbach, The steep redshift evolution of the hierarchical merger rate may cause the z - χ_{eff} correlation, (2026), arXiv:2601.03456 [astro-ph.HE].
- [9] A. Vijaykumar, A. M. Farah, and M. Fishbach, The maximum mass ratio of hierarchical mergers may cause the q - χ_{eff} correlation, (2026), arXiv:2601.03457 [astro-ph.HE].
- [10] O. Sridhar, A. Ray, and V. Kalogera, Characterizing Binary Black Hole Subpopulations in GWTC-4 with Binned Gaussian Processes: On the Origins of the $35M_{\odot}$ Peak, (2025), arXiv:2511.22093 [astro-ph.HE].
- [11] Y.-Z. Wang, Y.-J. Li, S.-J. Gao, S.-P. Tang, and Y.-Z. Fan, A new group of low-spin $50 - 70M_{\odot}$ Black Holes and the high pair-instability mass cutoff, (2025), arXiv:2510.22698 [astro-ph.HE].
- [12] S. Afroz and S. Mukherjee, Phase space of binary black holes from gravitational wave observations to unveil its formation history, *Phys. Rev. D* **112**, 023531 (2025), arXiv:2411.07304 [astro-ph.HE].
- [13] S. Afroz and S. Mukherjee, Binary Black Hole Phase Space Discovers the Signature of Pair Instability Supernovae Mass Gap, (2025), arXiv:2509.09123 [astro-ph.HE].
- [14] M. Zevin, S. S. Bavera, C. P. L. Berry, V. Kalogera, T. Fragos, P. Marchant, C. L. Rodriguez, F. Antonini, D. E. Holz, and C. Pankow, One Channel to Rule Them All? Constraining the Origins of Binary Black Holes Using Multiple Formation Pathways, *Astrophys. J.* **910**, 152 (2021), arXiv:2011.10057 [astro-ph.HE].
- [15] A. Q. Cheng, M. Zevin, and S. Vitale, What You Don't Know Can Hurt You: Use and Abuse of Astrophysical Models in Gravitational-wave Population Analyses, *Astrophys. J.* **955**, 127 (2023), arXiv:2307.03129 [astro-ph.HE].
- [16] S. Colloms, C. P. L. Berry, J. Veitch, and M. Zevin, Exploring the Evolution of Gravitational-wave Emitters with Efficient Emulation: Constraining the Origins of Binary Black Holes Using Normalizing Flows, *Astrophys. J.* **988**, 189 (2025), arXiv:2503.03819 [astro-ph.HE].
- [17] I. Mandel and F. S. Broekgaarden, Rates of compact object coalescences, *Living Rev. Rel.* **25**, 1 (2022), arXiv:2107.14239 [astro-ph.HE].
- [18] K. Breivik, Population Synthesis of Gravitational Wave Sources 10.1016/B978-0-443-21439-4.00115-2 (2025), arXiv:2502.03523 [astro-ph.HE].
- [19] I. Mandel and A. Farmer, Merging stellar-mass binary black holes, *Phys. Rept.* **955**, 1 (2022), arXiv:1806.05820 [astro-ph.HE].
- [20] M. Mapelli, Formation Channels of Single and Binary Stellar-Mass Black Holes (2021) arXiv:2106.00699 [astro-ph.HE].
- [21] D. Gerosa and M. Fishbach, Hierarchical mergers of stellar-mass black holes and their gravitational-wave signatures, *Nature Astron.* **5**, 749 (2021), arXiv:2105.03439 [astro-ph.HE].
- [22] J. Fuller, A. L. Piro, and A. S. Jermyn, Slowing the spins of stellar cores, *Mon. Not. Roy. Astron. Soc.* **485**, 3661 (2019), arXiv:1902.08227.
- [23] L. Ma and J. Fuller, Angular momentum transport in massive stars and natal neutron star rotation rates, *Mon. Not. Roy. Astron. Soc.* **488**, 4338 (2019), arXiv:1907.03713 [astro-ph.SR].
- [24] J. Fuller and L. Ma, Most Black Holes are Born Very Slowly Rotating, *Astrophys. J. Lett.* **881**, L1 (2019), arXiv:1907.03714 [astro-ph.SR].
- [25] S. S. Bavera *et al.*, The impact of mass-transfer physics on the observable properties of field binary black hole populations, *Astron. Astrophys.* **647**, A153 (2021), arXiv:2010.16333 [astro-ph.HE].
- [26] M. Zevin and S. S. Bavera, Suspicious Siblings: The Distribution of Mass and Spin across Component Black Holes in Isolated Binary Evolution, *Astrophys. J.* **933**, 86 (2022), arXiv:2203.02515 [astro-ph.HE].
- [27] F. S. Broekgaarden, S. Stevenson, and E. Thrane, Signatures of Mass Ratio Reversal in Gravitational Waves from Merging Binary Black Holes, *Astrophys. J.* **938**, 45 (2022), arXiv:2205.01693 [astro-ph.HE].
- [28] A. Heger and S. E. Woosley, The nucleosynthetic signature of population III, *Astrophys. J.* **567**, 532 (2002), arXiv:astro-ph/0107037.
- [29] S. E. Woosley, S. Blinnikov, and A. Heger, Pulsational pair instability as an explanation for the most luminous supernovae, *Nature* **450**, 390 (2007), arXiv:0710.3314 [astro-ph].
- [30] K. Belczynski *et al.*, The Effect of Pair-Instability Mass Loss on Black Hole Mergers, *Astron. Astrophys.* **594**, A97 (2016), arXiv:1607.03116 [astro-ph.HE].
- [31] M. Spera and M. Mapelli, Very massive stars, pair-instability supernovae and intermediate-mass black holes with the SEVN code, *Mon. Not. Roy. Astron. Soc.* **470**, 4739 (2017), arXiv:1706.06109 [astro-ph.SR].
- [32] R. Farmer, M. Renzo, S. E. de Mink, P. Marchant, and S. Justham, Mind the gap: The location of the lower edge of the pair instability supernovae black hole mass gap 10.3847/1538-4357/ab518b (2019), arXiv:1910.12874 [astro-ph.SR].
- [33] R. Farmer, M. Renzo, S. de Mink, M. Fishbach, and S. Justham, Constraints from gravitational wave detections of binary black hole mergers on the $^{12}\text{C}(\alpha, \gamma)^{16}\text{O}$ rate, *Astrophys. J. Lett.* **902**, L36 (2020), arXiv:2006.06678 [astro-ph.HE].
- [34] L. A. C. van Son, S. E. de Mink, F. S. Broekgaarden, M. Renzo, S. Justham, E. Laplace, J. Moran-Fraile, D. D. Hendriks, and R. Farmer, Polluting the pair-instability mass gap for binary black holes through super-Eddington accretion in isolated binaries, *Astrophys. J.* **897**, 100 (2020), arXiv:2004.05187 [astro-ph.HE].
- [35] J. Ziegler and K. Freese, Filling the black hole mass gap: Avoiding pair instability in massive stars through addition of nonnuclear energy, *Phys. Rev. D* **104**, 043015 (2021), arXiv:2010.00254 [astro-ph.HE].
- [36] D. D. Hendriks, L. A. C. van Son, M. Renzo, R. G. Izard, and R. Farmer, Pulsational pair-instability supernovae in gravitational-wave and electromagnetic transients, *Mon. Not. Roy. Astron. Soc.* **526**, 4130 (2023), arXiv:2309.09339 [astro-ph.HE].
- [37] E. Berti and M. Volonteri, Cosmological black hole spin evolution by mergers and accretion, *Astrophys. J.* **684**, 822 (2008), arXiv:0802.0025 [astro-ph].
- [38] F. Hofmann, E. Barausse, and L. Rezzolla, The final

- spin from binary black holes in quasi-circular orbits, *Astrophys. J. Lett.* **825**, L19 (2016), arXiv:1605.01938 [gr-qc].
- [39] C. L. Rodriguez, M. Zevin, P. Amaro-Seoane, S. Chatterjee, K. Kremer, F. A. Rasio, and C. S. Ye, Black holes: The next generation—repeated mergers in dense star clusters and their gravitational-wave properties, *Phys. Rev. D* **100**, 043027 (2019), arXiv:1906.10260 [astro-ph.HE].
- [40] A. Borchers, C. S. Ye, and M. Fishbach, Gravitational-wave Kicks Impact the Spins of Black Holes from Hierarchical Mergers, *Astrophys. J.* **987**, 10.3847/1538-4357/addec6 (2025), arXiv:2503.21278 [astro-ph.HE].
- [41] M. Fishbach, D. E. Holz, and B. Farr, Are LIGO’s Black Holes Made From Smaller Black Holes?, *Astrophys. J. Lett.* **840**, L24 (2017), arXiv:1703.06869 [astro-ph.HE].
- [42] R. M. O’Leary, F. A. Rasio, J. M. Fregeau, N. Ivanova, and R. W. O’Shaughnessy, Binary mergers and growth of black holes in dense star clusters, *Astrophys. J.* **637**, 937 (2006), arXiv:astro-ph/0508224.
- [43] F. Antonini and F. A. Rasio, Merging black hole binaries in galactic nuclei: implications for advanced-LIGO detections, *Astrophys. J.* **831**, 187 (2016), arXiv:1606.04889 [astro-ph.HE].
- [44] H. Tagawa, B. Kocsis, Z. Haiman, I. Bartos, K. Omukai, and J. Samsing, Mass-gap Mergers in Active Galactic Nuclei, *Astrophys. J.* **908**, 194 (2021), arXiv:2012.00011 [astro-ph.HE].
- [45] M. Mapelli *et al.*, Hierarchical black hole mergers in young, globular and nuclear star clusters: the effect of metallicity, spin and cluster properties, *Mon. Not. Roy. Astron. Soc.* **505**, 339 (2021), arXiv:2103.05016 [astro-ph.HE].
- [46] F. Antonini, M. Gieles, F. Dosopoulou, and D. Chattopadhyay, Coalescing black hole binaries from globular clusters: mass distributions and comparison to gravitational wave data from GWTC-3, *Mon. Not. Roy. Astron. Soc.* **522**, 466 (2023), arXiv:2208.01081 [astro-ph.HE].
- [47] S. Torniamenti, M. Mapelli, C. Périgois, M. A. Sedda, M. C. Artale, M. Dall’Amico, and M. P. Vaccaro, Hierarchical binary black hole mergers in globular clusters: Mass function and evolution with redshift, *Astron. Astrophys.* **688**, A148 (2024), arXiv:2401.14837 [astro-ph.HE].
- [48] M. P. Vaccaro, Hierarchical Black Hole Mergers in AGN Disks: Tracing Massive Black Hole Growth Across Cosmic Time, (2025), arXiv:2508.15337 [astro-ph.HE].
- [49] M. J. Fitchett, The influence of gravitational wave momentum losses on the centre of mass motion of a Newtonian binary system, *Mon. Not. Roy. Astron. Soc.* **203**, 1049 (1983).
- [50] S. F. Portegies Zwart and S. McMillan, Black hole mergers in the universe, *Astrophys. J. Lett.* **528**, L17 (2000), arXiv:astro-ph/9910061.
- [51] M. Favata, S. A. Hughes, and D. E. Holz, How black holes get their kicks: Gravitational radiation recoil revisited, *Astrophys. J. Lett.* **607**, L5 (2004), arXiv:astro-ph/0402056.
- [52] J. A. Gonzalez, U. Sperhake, B. Bruegmann, M. Hannam, and S. Husa, Total recoil: The Maximum kick from nonspinning black-hole binary inspiral, *Phys. Rev. Lett.* **98**, 091101 (2007), arXiv:gr-qc/0610154.
- [53] C. O. Lousto, H. Nakano, Y. Zlochower, and M. Campanelli, Statistical studies of Spinning Black-Hole Binaries, *Phys. Rev. D* **81**, 084023 (2010), [Erratum: *Phys. Rev. D* **82**, 129902 (2010)], arXiv:0910.3197 [gr-qc].
- [54] D. Gerosa, F. Hébert, and L. C. Stein, Black-hole kicks from numerical-relativity surrogate models, *Phys. Rev. D* **97**, 104049 (2018), arXiv:1802.04276 [gr-qc].
- [55] P. Mahapatra, A. Gupta, M. Favata, K. G. Arun, and B. S. Sathyaprakash, Remnant Black Hole Kicks and Implications for Hierarchical Mergers, *Astrophys. J. Lett.* **918**, L31 (2021), arXiv:2106.07179 [astro-ph.HE].
- [56] M. Zevin and D. E. Holz, Avoiding a Cluster Catastrophe: Retention Efficiency and the Binary Black Hole Mass Spectrum, *Astrophys. J. Lett.* **935**, L20 (2022), arXiv:2205.08549 [astro-ph.HE].
- [57] D. Gerosa and E. Berti, Are merging black holes born from stellar collapse or previous mergers?, *Phys. Rev. D* **95**, 124046 (2017), arXiv:1703.06223 [gr-qc].
- [58] C. Kimball, C. Talbot, C. P. L. Berry, M. Carney, M. Zevin, E. Thrane, and V. Kalogera, Black Hole Genealogy: Identifying Hierarchical Mergers with Gravitational Waves, *Astrophys. J.* **900**, 177 (2020), arXiv:2005.00023 [astro-ph.HE].
- [59] C. Kimball *et al.*, Evidence for Hierarchical Black Hole Mergers in the Second LIGO–Virgo Gravitational Wave Catalog, *Astrophys. J. Lett.* **915**, L35 (2021), arXiv:2011.05332 [astro-ph.HE].
- [60] C. Plunkett, T. Callister, M. Zevin, and S. Vitale, Signatures of a subpopulation of hierarchical mergers in the GWTC-4 gravitational-wave dataset, (2026), arXiv:2601.07908 [gr-qc].
- [61] H. Tong, T. A. Callister, M. Fishbach, E. Thrane, F. Antonini, S. Stevenson, I. M. Romero-Shaw, and F. Dosopoulou, A subpopulation of low-mass, spinning black holes: signatures of dynamical assembly, (2025), arXiv:2511.05316 [astro-ph.HE].
- [62] F. Antonini, I. M. Romero-Shaw, and T. Callister, Star Cluster Population of High Mass Black Hole Mergers in Gravitational Wave Data, *Phys. Rev. Lett.* **134**, 011401 (2025), arXiv:2406.19044 [astro-ph.HE].
- [63] F. Antonini, I. Romero-Shaw, T. Callister, F. Dosopoulou, D. Chattopadhyay, M. Gieles, and M. Mapelli, Gravitational waves reveal the pair-instability mass gap and constrain nuclear burning in massive stars, (2025), arXiv:2509.04637 [astro-ph.HE].
- [64] M. Mould, D. Gerosa, and S. R. Taylor, Deep learning and Bayesian inference of gravitational-wave populations: Hierarchical black-hole mergers, *Phys. Rev. D* **106**, 103013 (2022), arXiv:2203.03651 [astro-ph.HE].
- [65] A. Ray, I. Magaña Hernandez, K. Breivik, and J. Creighton, Searching for Binary Black Hole Subpopulations in Gravitational-wave Data Using Binned Gaussian Processes, *Astrophys. J.* **991**, 17 (2025), arXiv:2404.03166 [astro-ph.HE].
- [66] J. Sadiq, T. Dent, and D. Wysocki, Flexible and fast estimation of binary merger population distributions with an adaptive kernel density estimator, *Phys. Rev. D* **105**, 123014 (2022), arXiv:2112.12659 [gr-qc].
- [67] J. Sadiq, T. Dent, and M. Gieles, Binary Vision: The Mass Distribution of Merging Binary Black Holes via Iterative Density Estimation, *Astrophys. J.* **960**, 65 (2024), arXiv:2307.12092 [astro-ph.HE].
- [68] J. Godfrey, B. Edelman, and B. Farr, Cosmic Cousins: Identification of a Subpopulation of Binary Black Holes Consistent with Isolated Binary Evolution, (2023), arXiv:2304.01288 [astro-ph.HE].

- [69] S. K. Roy, L. A. C. van Son, and W. M. Farr, A mid-thirties crisis: dissecting the properties of gravitational wave sources near the 35 solar mass peak, *Class. Quant. Grav.* **42**, 225008 (2025), arXiv:2507.01086 [astro-ph.HE].
- [70] M. Mapelli, Y. Bouffanais, F. Santoliquido, M. A. Sedda, and M. C. Artale, The cosmic evolution of binary black holes in young, globular, and nuclear star clusters: rates, masses, spins, and mixing fractions, *Mon. Not. Roy. Astron. Soc.* **511**, 5797 (2022), arXiv:2109.06222 [astro-ph.HE].
- [71] D. Chattopadhyay, J. Stegmann, F. Antonini, J. Barber, and I. M. Romero-Shaw, Double black hole mergers in nuclear star clusters: eccentricities, spins, masses, and the growth of massive seeds, *Mon. Not. Roy. Astron. Soc.* **526**, 4908 (2023), arXiv:2308.10884 [astro-ph.HE].
- [72] C. L. Rodriguez, N. C. Weatherford, S. C. Coughlin, P. Amaro-Seoane, K. Breivik, S. Chatterjee, G. Fragione, F. Kiroglu, K. Kremer, N. Z. Rui, C. S. Ye, M. Zevin, and F. A. Rasio, Modeling dense star clusters in the milky way and beyond with the cluster monte carlo code, *The Astrophysical Journal Supplement Series* **258**, 22 (2022).
- [73] F. Kiroglu, J. C. Lombardi, K. Kremer, H. D. Vanderzypden, and F. A. Rasio, Spin-Orbit Alignment in Merging Binary Black Holes Following Collisions with Massive Stars, *Astrophys. J. Lett.* **983**, L9 (2025), arXiv:2501.09068 [astro-ph.HE].
- [74] H. Tagawa, Z. Haiman, I. Bartos, and B. Kocsis, Spin Evolution of Stellar-mass Black Hole Binaries in Active Galactic Nuclei, *Astrophys. J.* **899**, 26 (2020), arXiv:2004.11914 [astro-ph.HE].
- [75] B. McKernan, K. E. S. Ford, T. Callister, W. M. Farr, R. O’Shaughnessy, R. Smith, E. Thrane, and A. Vajpeyi, LIGO–Virgo correlations between mass ratio and effective inspiral spin: testing the active galactic nuclei channel, *Mon. Not. Roy. Astron. Soc.* **514**, 3886 (2022), arXiv:2107.07551 [astro-ph.HE].
- [76] G. Li, H. G. Bhaskar, B. Kocsis, and D. N. C. Lin, Secular Spin-Orbit Resonances of Black Hole Binaries in AGN Disks, *Astrophys. J.* **950**, 48 (2023), arXiv:2202.11739 [astro-ph.HE].
- [77] B. McKernan *et al.*, Constraining Stellar-mass Black Hole Mergers in AGN Disks Detectable with LIGO, *Astrophys. J.* **866**, 66 (2018), arXiv:1702.07818 [astro-ph.HE].
- [78] A. Santini, D. Gerosa, R. Cotesta, and E. Berti, Black-hole mergers in disklike environments could explain the observed q - χ_{eff} correlation, *Phys. Rev. D* **108**, 083033 (2023), arXiv:2308.12998 [astro-ph.HE].
- [79] B. McKernan and K. E. S. Ford, Constraining the LVK AGN channel with black hole spins, *Mon. Not. Roy. Astron. Soc.* **531**, 3479 (2024), arXiv:2309.15213 [astro-ph.HE].
- [80] B. McKernan, K. E. S. Ford, H. E. Cook, V. Delfavero, E. McPike, K. Nathaniel, J. Postiglione, S. Ray, and R. O’Shaughnessy, McFACTS I: Testing the LVK AGN Channel with Monte Carlo for AGN Channel Testing and Simulation (McFACTS), *Astrophys. J.* **990**, 217 (2025), arXiv:2410.16515 [astro-ph.HE].
- [81] H. E. Cook, B. McKernan, K. E. S. Ford, V. Delfavero, K. Nathaniel, J. Postiglione, S. Ray, E. J. McPike, and R. O’Shaughnessy, McFACTS. II. Mass Ratio–Effective Spin Relationship of Black Hole Mergers in the Active Galactic Nucleus Channel, *Astrophys. J.* **993**, 163 (2025), arXiv:2411.10590 [astro-ph.HE].
- [82] G. Fabj, C. Tiede, C. Rowan, M. Pessah, and J. Samsing, Spin-Orbit Misalignments of Eccentric Black Hole Mergers in AGN Disks, (2025), arXiv:2510.07952 [astro-ph.HE].
- [83] F. Antonini, S. Toonen, and A. S. Hamers, Binary black hole mergers from field triples: properties, rates and the impact of stellar evolution, *Astrophys. J.* **841**, 77 (2017), arXiv:1703.06614 [astro-ph.GA].
- [84] B. Liu and D. Lai, Black Hole and Neutron Star Binary Mergers in Triple Systems: Merger Fraction and Spin–Orbit Misalignment, *Astrophys. J.* **863**, 68 (2018), arXiv:1805.03202 [astro-ph.HE].
- [85] C. L. Rodriguez and F. Antonini, A Triple Origin for the Heavy and Low-Spin Binary Black Holes Detected by LIGO/Virgo, *Astrophys. J.* **863**, 7 (2018), arXiv:1805.08212 [astro-ph.HE].
- [86] V. Kalogera, Spin orbit misalignment in close binaries with two compact objects, *Astrophys. J.* **541**, 319 (2000), arXiv:astro-ph/9911417.
- [87] S. S. Bavera, T. Fragos, Y. Qin, E. Zapartas, C. J. Neijssel, I. Mandel, A. Batta, S. M. Gaebel, C. Kimball, and S. Stevenson, The origin of spin in binary black holes: Predicting the distributions of the main observables of Advanced LIGO, *Astron. Astrophys.* **635**, A97 (2020), arXiv:1906.12257 [astro-ph.HE].
- [88] D. Gerosa, E. Berti, R. O’Shaughnessy, K. Belczynski, M. Kesden, D. Wysocki, and W. Gladysz, Spin orientations of merging black holes formed from the evolution of stellar binaries, *Phys. Rev. D* **98**, 084036 (2018), arXiv:1808.02491 [astro-ph.HE].
- [89] N. Steinle and M. Kesden, Signatures of spin precession and nutation in isolated black-hole binaries, *Phys. Rev. D* **106**, 063028 (2022), arXiv:2206.00391 [astro-ph.HE].
- [90] L. S. Collaboration, V. Collaboration, and K. Collaboration, Gwtc-4.0 cumulative search sensitivity estimates, 10.5281/zenodo.16740128 (2025).
- [91] L. S. Collaboration, V. Collaboration, and K. Collaboration, Gwtc-3: Compact binary coalescences observed by ligo and virgo during the second part of the third observing run — parameter estimation data release, 10.5281/zenodo.5546663 (2021).
- [92] L. S. Collaboration and V. Collaboration, Gwtc-2.1: Deep extended catalog of compact binary coalescences observed by ligo and virgo during the first half of the third observing run - parameter estimation data release, 10.5281/zenodo.6513631 (2022).
- [93] L. S. Collaboration, V. Collaboration, and K. Collaboration, Gwtc-4.0: Parameter estimation data release, 10.5281/zenodo.16053484 (2025).
- [94] R. Abbott *et al.* (LIGO Scientific, Virgo), Open data from the first and second observing runs of Advanced LIGO and Advanced Virgo, *SoftwareX* **13**, 100658 (2021), arXiv:1912.11716 [gr-qc].
- [95] A. G. Abac *et al.* (LIGO Scientific, VIRGO, KAGRA), Open Data from LIGO, Virgo, and KAGRA through the First Part of the Fourth Observing Run, (2025), arXiv:2508.18079 [gr-qc].
- [96] R. Abbott *et al.* (KAGRA, VIRGO, LIGO Scientific), Open Data from the Third Observing Run of LIGO, Virgo, KAGRA, and GEO, *Astrophys. J. Suppl.* **267**, 29 (2023), arXiv:2302.03676 [gr-qc].
- [97] T. J. Loredo, Accounting for source uncertainties in

- analyses of astronomical survey data, in *AIP Conference Proceedings* (AIP, 2004).
- [98] D. Wysocki, J. Lange, and R. O’Shaughnessy, Reconstructing phenomenological distributions of compact binaries via gravitational wave observations, *Phys. Rev. D* **100**, 043012 (2019).
- [99] S. Vitale, D. Gerosa, W. M. Farr, and S. R. Taylor, Inferring the properties of a population of compact binaries in presence of selection effects 10.1007/978-981-15-4702-7_45-1 (2020), arXiv:2007.05579 [astro-ph.IM].
- [100] W. M. Farr, Accuracy requirements for empirically measured selection functions, *Research Notes of the AAS* **3**, 66 (2019).
- [101] R. Essick and W. Farr, Precision requirements for monte carlo sums within hierarchical bayesian inference (2022), arXiv:2204.00461 [astro-ph.IM].
- [102] E. Thrane and C. Talbot, An introduction to Bayesian inference in gravitational-wave astronomy: parameter estimation, model selection, and hierarchical models, *Publ. Astron. Soc. Austral.* **36**, e010 (2019), [Erratum: *Publ. Astron. Soc. Austral.* **37**, e036 (2020)], arXiv:1809.02293 [astro-ph.IM].
- [103] H. Tong *et al.*, Evidence of the pair instability gap in the distribution of black hole masses, (2025), arXiv:2509.04151 [astro-ph.HE].
- [104] M. Fishbach, C. Kimball, and V. Kalogera, Limits on Hierarchical Black Hole Mergers from the Most Negative χ_{eff} Systems, *Astrophys. J. Lett.* **935**, L26 (2022), arXiv:2207.02924 [astro-ph.HE].
- [105] S. Vitale and M. Mould (Society of Physicists Interested in Non-aligned Spins, SPINS, (Society of Physicists Interested in Non-aligned Spins, SPINS)†), Long road to alignment: Measuring black hole spin orientation with expanding gravitational-wave datasets, *Phys. Rev. D* **112**, 083015 (2025), arXiv:2505.14875 [astro-ph.HE].
- [106] D. Wysocki, D. Gerosa, R. O’Shaughnessy, K. Belczynski, W. Gladysz, E. Berti, M. Kesden, and D. E. Holz, Explaining LIGO’s observations via isolated binary evolution with natal kicks, *Phys. Rev. D* **97**, 043014 (2018), arXiv:1709.01943 [astro-ph.HE].
- [107] T. A. Callister, W. M. Farr, and M. Renzo, State of the Field: Binary Black Hole Natal Kicks and Prospects for Isolated Field Formation after GWTC-2, *Astrophys. J.* **920**, 157 (2021), arXiv:2011.09570 [astro-ph.HE].
- [108] G. Fragione, A. Loeb, and F. A. Rasio, Impact of Natal Kicks on Merger Rates and Spin–Orbit Misalignments of Black Hole–Neutron Star Mergers, *Astrophys. J. Lett.* **918**, L38 (2021), arXiv:2108.06538 [astro-ph.HE].
- [109] I. Mandel, Estimates of black-hole natal kick velocities from observations of low-mass X-ray binaries, *Mon. Not. Roy. Astron. Soc.* **456**, 578 (2016), arXiv:1510.03871 [astro-ph.HE].
- [110] F. Mirabel, The Formation of Stellar Black Holes, *New Astron. Rev.* **78**, 1 (2017), arXiv:1609.08411 [astro-ph.HE].
- [111] T. M. Tauris, Tossing Black Hole Spin Axes, *Astrophys. J.* **938**, 66 (2022), arXiv:2205.02541 [astro-ph.HE].
- [112] M. M. Briel, H. F. Stevance, and J. J. Eldridge, Understanding the high-mass binary black hole population from stable mass transfer and super-Eddington accretion in bpass, *Mon. Not. Roy. Astron. Soc.* **520**, 5724 (2023), arXiv:2206.13842 [astro-ph.HE].
- [113] S. E. de Mink and I. Mandel, The chemically homogeneous evolutionary channel for binary black hole mergers: rates and properties of gravitational-wave events detectable by advanced LIGO, *Mon. Not. Roy. Astron. Soc.* **460**, 3545 (2016), arXiv:1603.02291 [astro-ph.HE].
- [114] F. Kiroğlu, K. Kremer, S. Biscoveanu, E. G. Prieto, and F. A. Rasio, Black Hole Accretion and Spin-up through Stellar Collisions in Dense Star Clusters, *Astrophys. J.* **979**, 237 (2025), arXiv:2410.01879 [astro-ph.HE].
- [115] C. L. Rodriguez, M. Zevin, C. Pankow, V. Kalogera, and F. A. Rasio, Illuminating Black Hole Binary Formation Channels with Spins in Advanced LIGO, *Astrophys. J. Lett.* **832**, L2 (2016), arXiv:1609.05916 [astro-ph.HE].
- [116] W. M. Farr, S. Stevenson, M. Coleman Miller, I. Mandel, B. Farr, and A. Vecchio, Distinguishing Spin-Aligned and Isotropic Black Hole Populations With Gravitational Waves, *Nature* **548**, 426 (2017), arXiv:1706.01385 [astro-ph.HE].
- [117] F. Antonini, M. Gieles, F. Dosopoulou, and D. Chattohadhyay, Coalescing black hole binaries from globular clusters: mass distributions and comparison to gravitational wave data from gwtc-3, *Monthly Notices of the Royal Astronomical Society* **522**, 466 (2023), <https://academic.oup.com/mnras/article-pdf/522/1/466/49913333/stad972.pdf>.
- [118] D. C. Heggie, Star cluster simulations, (1997), arXiv:astro-ph/9711185.
- [119] J. Stegmann, F. Antonini, A. Olejak, S. Biscoveanu, V. Raymond, S. Rinaldi, and B. Flanagan, In-plane Black-hole Spin Measurements Suggest Most Gravitational-wave Mergers Form in Triples, (2025), arXiv:2512.15873 [astro-ph.HE].
- [120] E. Farag, M. Renzo, R. Farmer, M. T. Chidester, and F. X. Timmes, Resolving the Peak of the Black Hole Mass Spectrum, *Astrophys. J.* **937**, 112 (2022), arXiv:2208.09624 [astro-ph.HE].
- [121] C. Angulo, M. Arnould, M. Rayet, P. Descouvemont, D. Baye, C. Leclercq-Willain, A. Coc, S. Barhoumi, P. Aguer, C. Rolfs, R. Kunz, J. W. Hammer, A. Mayer, T. Paradellis, S. Kossionides, C. Chronidou, K. Spyrou, S. degl’Innocenti, G. Fiorentini, B. Ricci, S. Zavatarelli, C. Providencia, H. Wolters, J. Soares, C. Grama, J. Rahighi, A. Shotton, and M. Laméhi Rachti, A compilation of charged-particle induced thermonuclear reaction rates, *nphysa* **656**, 3 (1999).
- [122] L. A. C. van Son, S. E. de Mink, M. Renzo, S. Justham, E. Zapartas, K. Breivik, T. Callister, W. M. Farr, and C. Conroy, No Peaks without Valleys: The Stable Mass Transfer Channel for Gravitational-wave Sources in Light of the Neutron Star–Black Hole Mass Gap, *Astrophys. J.* **940**, 184 (2022), arXiv:2209.13609 [astro-ph.HE].
- [123] A. Olejak, J. Klencki, X.-T. Xu, C. Wang, K. Belczynski, and J.-P. Lasota, Unequal-mass, highly-spinning binary black hole mergers in the stable mass transfer formation channel, *Astron. Astrophys.* **689**, A305 (2024), arXiv:2404.12426 [astro-ph.HE].
- [124] A. Dorozsmai and S. Toonen, Importance of stable mass transfer and stellar winds for the formation of gravitational wave sources, *Mon. Not. Roy. Astron. Soc.* **530**, 3706 (2024), arXiv:2207.08837 [astro-ph.SR].
- [125] T. Bruel, A. Lamberts, C. L. Rodriguez, R. Feldmann, M. Y. Grudic, and J. Moreno, Great Balls of FIRE - IV. Contribution of massive star clusters to the astrophysical population of merging binary black holes, *Astron. Astrophys.* **701**, A252 (2025), arXiv:2503.03810 [astro-

- ph.GA].
- [126] C. S. Ye and M. Fishbach, The Redshift Evolution of the Binary Black Hole Mass Distribution from Dense Star Clusters, *Astrophys. J.* **967**, 62 (2024), arXiv:2402.12444 [astro-ph.HE].
- [127] A. Mai, K. Kremer, and F. Kiroğlu, Shadows of the Colossus: Hierarchical Black Hole Mergers in a 10-million-body Globular Cluster Simulation, *Astrophys. J.* **998**, 138 (2026), arXiv:2510.21916 [astro-ph.GA].
- [128] R. J. deBoer *et al.*, The $^{12}\text{C}(\alpha,\gamma)^{16}\text{O}$ reaction and its implications for stellar helium burning, *Rev. Mod. Phys.* **89**, 035007 (2017), arXiv:1709.03144 [nucl-ex].
- [129] M. Fishbach, D. E. Holz, and W. M. Farr, Does the Black Hole Merger Rate Evolve with Redshift?, *Astrophys. J. Lett.* **863**, L41 (2018), arXiv:1805.10270 [astro-ph.HE].
- [130] I. Mandel, W. M. Farr, and J. R. Gair, Extracting distribution parameters from multiple uncertain observations with selection biases, *Mon. Not. Roy. Astron. Soc.* **486**, 1086 (2019), arXiv:1809.02063 [physics.data-an].
- [131] C. Talbot, A. Farah, S. Galaudage, J. Golomb, and H. Tong, Gwpopulation: Hardware agnostic population inference for compact binaries and beyond, *Journal of Open Source Software* **10**, 7753 (2025), arXiv:2409.14143 [astro-ph.IM].
- [132] D. Wysocki, J. Lange, and R. O’Shaughnessy, Exploring short gamma-ray burst progenitors with gravitational waves, *Physical Review D* **100**, 043012 (2019).
- [133] C. Talbot and J. Golomb, Growing pains: understanding the impact of likelihood uncertainty on hierarchical Bayesian inference for gravitational-wave astronomy, *Mon. Not. Roy. Astron. Soc.* **526**, 3495 (2023), arXiv:2304.06138 [astro-ph.IM].
- [134] J. Skilling, Nested sampling for general Bayesian computation, *Bayesian Analysis* **1**, 833 (2006).
- [135] C. Talbot, R. Smith, E. Thrane, and G. B. Poole, Parallelized inference for gravitational-wave astronomy, *Phys. Rev. D* **100**, 043030 (2019), arXiv:1904.02863 [astro-ph.IM].
- [136] M. Fishbach, W. M. Farr, and D. E. Holz, The Most Massive Binary Black Hole Detections and the Identification of Population Outliers, *Astrophys. J. Lett.* **891**, L31 (2020), arXiv:1911.05882 [astro-ph.HE].
- [137] T. A. Callister and W. M. Farr, Parameter-Free Tour of the Binary Black Hole Population, *Phys. Rev. X* **14**, 021005 (2024), arXiv:2302.07289 [astro-ph.HE].
- [138] S. J. Miller, Z. Ko, T. Callister, and K. Chatziioannou, Gravitational waves carry information beyond effective spin parameters but it is hard to extract, *Phys. Rev. D* **109**, 104036 (2024), arXiv:2401.05613 [gr-qc].
- [139] P. Madau and M. Dickinson, Cosmic Star Formation History, *Ann. Rev. Astron. Astrophys.* **52**, 415 (2014), arXiv:1403.0007 [astro-ph.CO].
- [140] J. Heinzl, M. Mould, and S. Vitale, Nonparametric analysis of correlations in the binary black hole population with LIGO-Virgo-KAGRA data, *Phys. Rev. D* **111**, L061305 (2025), arXiv:2406.16844 [astro-ph.HE].
- [141] A. Ray, I. Magaña Hernandez, S. Mohite, J. Creighton, and S. Kapadia, Nonparametric Inference of the Population of Compact Binaries from Gravitational-wave Observations Using Binned Gaussian Processes, *Astrophys. J.* **957**, 37 (2023), arXiv:2304.08046 [gr-qc].
- [142] R. Abbott *et al.* (KAGRA, VIRGO, LIGO Scientific), Population of Merging Compact Binaries Inferred Using Gravitational Waves through GWTC-3, *Phys. Rev. X* **13**, 011048 (2023), arXiv:2111.03634 [astro-ph.HE].
- [143] J. Stegmann, F. Antonini, and M. Moe, Evolution of massive stellar triples and implications for compact object binary formation, *Mon. Not. Roy. Astron. Soc.* **516**, 1406 (2022), arXiv:2112.10786 [astro-ph.SR].
- [144] V. Tiwari, Population of Binary Black Holes Inferred from One Hundred and Fifty Gravitational Wave Signals, (2025), arXiv:2510.25579 [astro-ph.HE].
- [145] V. Tiwari, Exploring Features in the Binary Black Hole Population, *Astrophys. J.* **928**, 155 (2022), arXiv:2111.13991 [astro-ph.HE].
- [146] V. Tiwari and S. Fairhurst, The Emergence of Structure in the Binary Black Hole Mass Distribution, *Astrophys. J. Lett.* **913**, L19 (2021), arXiv:2011.04502 [astro-ph.HE].

SUPPLEMENTAL MATERIAL

Here, we present detailed methodologies, additional results, and demonstrations that supplement and validate the findings delineated in the main body of this *Letter*. In particular, we present (in order):

1. Details of our population analysis framework,
2. Model comparison studies: variations in functional forms and priors,
3. Variation of astrophysical metrics with functional forms and priors,
4. Prior-predictive distributions,
5. Additional tests of model misspecification,
6. Comparison of marginal distributions and mass-based transitions with the previous findings of data-driven analyses, and
7. A demonstration of how properties of the effective spin distribution can elucidate astrophysically crucial trends in the population properties of component spin magnitudes and orientations.

Population Analysis — The results presented in this work were obtained through Bayesian hierarchical inference using a three-component mixture model for the joint distribution of BBH primary masses (m_1), mass ratios (q), effective aligned (χ_{eff}) and precessing (χ_p) spins, and redshifts (z), which takes the following form:

$$\frac{dN}{dm_1 dq d\chi_{eff} d\chi_p dz}(\vec{\Lambda}) = R_0 \frac{dV}{dz} \frac{T_{obs}}{1+z} \sum_{i=1}^3 f_i p_i(q|m_1, \vec{\Lambda}_q^i) p_i(m_1|\vec{\Lambda}_m^i) p_i(\chi_{eff}, \chi_p|\vec{\Lambda}_\chi^i) (1+z)^{\kappa_i}, \quad (1)$$

where R_0 is the local rate per comoving volume (V) and source-frame time ($\frac{T_{obs}}{1+z}$), f_i is the branching fraction of the formation channel contributing dominantly to the i th component, and κ_i its corresponding redshift evolution parameter [129]. Here, $\vec{\Lambda}_\theta^i$ represents additional hyperparameters that control the shape of the distribution function of the BBH parameter θ for the i th component. Our mixture components are constructed from simple functional forms, which are delineated in the next section. See also Refs. [144–146], who use generic mixture models for a flexible reconstruction of the joint BBH population distribution.

We constrain our distributions by modeling the occurrence of BBH mergers as an inhomogeneous Poisson process [102, 130, 132]. We construct the likelihood function of population hyperparameters using individual event parameter estimation data for all GWTC-4 BBH candidates found with a false alarm rate of less than 1 per year. We use the exact same PE samples used by Ref. [5], which are delineated in their section 3.4. We rely on simulated signals injected into detector noise realizations to correct for Malmquist biases that might result from the choice of a stringent detection criterion. Using publicly released LVK data for single event PE runs and detectable injections, we constrain the posterior distribution of population hyperparameters and compute the Bayesian evidence in favour of model assumptions by means of nested sampling techniques [134]. We ensure the convergence of Monte Carlo sums used to construct our likelihood function using the standard variance-based penalty proposed by Ref. [133]. We rely on the `gwpopulation` library [131, 135] for implementing our hierarchical inference. The code developed to implement this analysis will be made publicly available after the acceptance of this manuscript, and, in the meantime, will be shared upon reasonable request.

Model Comparison: Functional Forms & Hyperpriors

— We now explore model variations to investigate the prior dependence of our results. Our mixture components are constructed from simple parametrizations such as powerlaws (PL), smoothed powerlaws (SPL), smoothed broken power laws (BPL), smoothed broken power laws + Gaussian peak (BPLP), smoothed power laws mixed with Gaussian peaks (PLP), truncated Gaussians (\mathcal{N}), and uniform distributions (U) which are expressed below:

$$\text{PL}_{a,b}^\alpha(x) = \begin{cases} \frac{(1+\alpha)x^\alpha}{b^{1+\alpha}-a^{1+\alpha}}, & a \leq x \leq b \\ 0, & o.w. \end{cases} \quad (2)$$

$$\text{SPL}_{a,b}^{\alpha,\delta}(x) \propto S(x, a, b, \delta_m) \text{PL}_{a,b}^\alpha(x) \quad (3)$$

$$\mathcal{N}_{a,b}^{\mu,\sigma}(x) \propto \begin{cases} e^{-\frac{1}{2}\left(\frac{x-\mu}{\sigma}\right)^2}, & a \leq x \leq b \\ 0, & o.w. \end{cases} \quad (4)$$

$$U_{a,b}(x) = \begin{cases} \frac{1}{b-a}, & a \leq x \leq b \\ 0, & o.w. \end{cases} \quad (5)$$

$$\text{PLP}_{a,b}^{\alpha,\delta,\lambda,\mu,\sigma}(x) = (1-\lambda)\text{SPL}_{a,b}^{\alpha,\delta}(x) + \lambda\mathcal{N}_{a,b}^{\mu,\sigma}(x) \quad (6)$$

$$\text{BPL}_{a,b}^{\alpha_1,\alpha_2,x_b,\delta}(x) \propto S(x, a, b, \delta_m) \begin{cases} \text{PL}_{a,x_b}^{\alpha_1}(x) \frac{\text{PL}_{a,x_b}^{\alpha_1}(x_b)}{\text{PL}_{x_b,b}^{\alpha_2}(x_b)}, & x \leq x_b, \\ \text{PL}_{x_b,b}^{\alpha_2}(x), & o.w. \end{cases} \quad (7)$$

and,

$$\text{BPLP}_{a,b}^{\alpha_1,\alpha_2,x_b,\delta,\lambda,\mu,\sigma}(x) = (1-\lambda)\text{BPL}_{a,b}^{\alpha_1,\alpha_2,x_b,\delta}(x) + \lambda\mathcal{N}_{a,b}^{\mu,\sigma}(x) \quad (8)$$

where,

$$S(x, a, b, \delta) = \frac{1}{1 + e^{\frac{\delta}{\delta-x+a} - \frac{\delta}{x-a}}} \quad (9)$$

is a smoothing window for the turn on of power laws. Note that the constants of proportionality are derived by imposing that each distribution function is normalized. For our most preferred model, the functional forms chosen for each component's distribution functions were listed in the main text (Table I). We also define a Broken Powerlaw plus two Gaussian peaks BPL2P mass function, which is the default distribution of Ref. [5], used as a benchmark for our model comparison studies, as follows:

$$\text{BPL2P}_{a,b}^{\alpha_1,\alpha_2,x_b,\delta,\lambda_1,\mu_1,\sigma_1,\lambda_2,\mu_2,\sigma_2}(x) = \lambda_1\mathcal{N}_{a,b}^{\mu_1,\sigma_1}(x) + (1-\lambda_1)\text{BPLP}_{a,b}^{\alpha_1,\alpha_2,x_b,\delta,\lambda_2,\mu_2,\sigma_2}(x). \quad (10)$$

We explore several variations which are listed (along with their Bayes factors and changes in maximum log likelihood, both with respect to the default model that does not allow for subpopulations) in Table V. For each model, we have explored further variations in the choices of hyperpriors. The Bayes factors represented in Table V correspond to the most preferred hyperprior choice for each set of functional forms.

With models II and III, we explore how the inferred shapes of $p_i(m_1)$ depend on the choice of functional

forms. In particular, with II, we verify whether the $35M_{\odot}$ feature can be well described with a change in the powerlaw index or if it requires an additional Gaussian to account for the overabundance. In III, we explore whether the same functional form of $p(m_1)$ for all three components is preferred by the data over our specific choices in I. With model IV, we explore whether the mass-ratio distribution of component 2 is equally well described by a truncated Gaussian similar to components 1 and 3, or if it necessitates the Powerlaw as chosen for I. Finally, with models V and VI, we verify whether the $p(\chi_{eff})$ of component III is better described by a Gaussian or a more flexible Uniform distribution as compared to our choice in I. In all these variations, we find that the data either prefer Model I or are unable to distinguish between the deviations from Model I.

We next turn to variations in hyperpriors for our most preferred model. We start by listing all the hyperpriors that have the highest Bayes factors in Table VI, along with the prior predictive and posterior predictive credible intervals for each free hyperparameter. As mentioned in the main text, we target the subpopulation of hierarchical mergers with component 3 without enforcing its existence. However, additional restrictions were imposed for components 1 and 2 in Table VI. In Table VII we list flexible alternatives for these strongly restrictive hyperpriors along with the corresponding Bayes factors and changes in maximum log likelihood with respect to the default model. It can be seen that relaxing prior restrictions either does not change the inferred values of the corresponding hyperparameter or leads to an increase in prior volume without any change in the maximum likelihood. In other words, the hyperparameters that were fixed in the most preferred prior choice, when allowed to vary, are mostly uninformative over the prior range, leading to comparable shapes in the inferred distributions and slightly smaller or comparable Bayes factors.

Additional hyperpriors for models II-VI are presented in Tables VIII, IX, X, XI, and XII respectively.

Variation of astrophysical metrics with functional forms & priors — We now demonstrate that the metrics used to establish our astrophysical interpretation, which are summarized in Table III of the main text, are robust against variations in modeling assumptions. First, we compare the inferred values of $\sigma_{\chi_{eff}}^3$, $P_3(\chi_{eff} < 0)$ and $P_3(q > 0.7)$ obtained using model I with those that employ much more flexible functional forms and/or hyperpriors for the corresponding distributions, namely models II, V, and VI. We show in Figure 3 that more flexible modeling assumptions lead to values consistent with the ones presented in the main text, with the only difference being an expected increase in measurement uncertainty. In other words, our conclusions regarding Comp. 3 remain unchanged upon lifting certain restrictions previously employed for targeting the hierarchical subpopulation.

In addition to these metrics for Comp. 3, we also explore variations in $P(q > 0.7)$ for Comp. 2. Since Comp. 2 is the only one with a PL mass-ratio distribution, as compared to the truncated Gaussians used with the other two components, we investigate whether or not $P_2(q > 0.7)$ is affected by this choice of $p_2(q)$. We hence compare the inferred values of $P_2(q > 0.7)$ obtained using Model I and Model IV. We show in Figure 4 that despite being strongly disfavoured by the data, model IV is consistent with model I's measurement of the fraction of systems with $q > 0.7$ that was presented in the main text.

We note here that the other astrophysically informative metrics for Comp. 1 and Comp. 2 are unlikely to be affected by strong modeling assumptions since the corresponding distributions are reasonably flexible. Furthermore, we find our results to be consistent with data-driven reconstructions of the joint distribution of BBH parameters (as we show later on), indicating that the inferred conclusions are likely not driven by prior assumptions.

Prior Predictive Draws — We now turn to comparisons of our inferred distributions for the most preferred model, to those corresponding to the prior predictive draws of hyperparameters. In Figure 5, it can be seen that the posterior is more informative than the prior for each distribution function and hyperparameter. Coupled with our model comparison results presented before, this indicates that our conclusions are driven by the data and not by modeling assumptions. We later on compare, where available, the marginal distributions of some BBH parameters conditioned on others, with corresponding data-driven reconstructions, to show that our results are consistent with flexible analyses that impose very few modeling assumptions.

Posterior Predictive Checks — Next, we look for additional signatures of model-misspecification in our analysis by performing posterior predictive checks [136–138]. We start by reweighting the posterior of each individual BBH's parameters to the population-informed prior, as displayed in Figure 6. It can be seen that clusters identical to the subpopulations identified in the main text appear in each combination of observed BBH parameters. We then compare draws from this reweighted sample of observations to the posterior predictive population of detections. The latter is obtained by reweighting the detectable simulations, which were used to estimate selection effects, to the population-informed prior. As shown in Figure 7, the traces corresponding to each draw are concentrated about the diagonal, indicating no signatures of systemic model misspecification.

Marginal Distributions and Transitions — Finally, we show that our reconstructed distributions are consistent with alternative analyses that either do not account for subpopulations (such as the default case) or search for mass-based transitions in the distribution of other

Model	Comp.	$p(m_1)$	$p(q m_1)$	$p(\chi_{eff})$	$p(\chi_p)$	$\log_{10} BF$	$\Delta \log \mathcal{L}_{max}$
I	1	$\text{PLP}_{m_1, \min, m_1, \max}^{\alpha_m^1, \delta_m, \lambda_m^1, \mu_m^1, \sigma_m^1}$	$\mathcal{N}_{\frac{m_2, \min, 1}{m_1}}^{\mu_q^1, \sigma_q^1}$	$\mathcal{N}_{-1, 1}^{\mu_{\chi_{eff}}^1, \sigma_{\chi_{eff}}^1}$	$\mathcal{N}_{0, 1}^{\mu_{\chi_p}^1, \sigma_{\chi_p}^1}$	6	24
	2	$\text{BPL}_{m_1, \min, m_1, \max}^{\alpha_m^2, \delta_m, \lambda_m^2, \mu_m^2, \sigma_m^2}$	$\text{PL}_{\frac{m_2, \min, 1}{m_1}}^{\beta_q^2, \frac{\sigma_m^2}{m_1}}$	$\mathcal{N}_{-1, 1}^{\mu_{\chi_{eff}}^2, \sigma_{\chi_{eff}}^2}$	$\mathcal{N}_{0, 1}^{\mu_{\chi_p}^2, \sigma_{\chi_p}^2}$		
	3	$\text{BLP}_{m_1, \min, m_1, \max}^{\alpha_m^3, \delta_m, \lambda_m^3, \mu_m^3, \sigma_m^3}$	$\mathcal{N}_{\frac{m_2, \min, 1}{m_1}}^{\mu_q^3, \sigma_q^3}$	$U_{-w^3, w^3}^{\chi_{eff}^3, w_{\chi_{eff}}^3}$	$\mathcal{N}_{0, 1}^{\mu_{\chi_p}^3, \sigma_{\chi_p}^3}$		
II	1	Same as I	Same as I	Same as I	Same as I	6	23
	2	$\text{BPLP}_{m_1, \min, m_1, \max}^{\alpha_m^2, \delta_m, \lambda_m^2, \mu_m^2, \sigma_m^2, \lambda_m^2, \mu_m^2, \sigma_m^2}$	Same as I	Same as I	Same as I		
	3	Same as I	Same as I	Same as I	Same as I		
III	1	Same as I	Same as I	Same as I	Same as I	5.6	22.7
	2	$\text{PLP}_{m_1, \min, m_1, \max}^{\alpha_m^2, \delta_m, \lambda_m^2, \mu_m^2, \sigma_m^2}$	Same as I	Same as I	Same as I		
	3	$\text{PLP}_{m_1, \min, m_1, \max}^{\alpha_m^3, \delta_m, \lambda_m^3, \mu_m^3, \sigma_m^3}$	Same as I	Same as I	Same as I		
IV	1	Same as I	Same as I	Same as I	Same as I	6	23
	2	Same as I	$\mathcal{N}_{\frac{m_2, \min, 1}{m_1}}^{\mu_q^2, \sigma_q^2}$	Same as I	Same as I		
	3	Same as I	Same as I	Same as I	Same as I		
V	1	Same as I	Same as I	Same as I	Same as I	6	23
	2	Same as I	Same as I	Same as I	Same as I		
	3	Same as I	Same as I	$U_{a^3, b^3}^{\chi_{eff}^3, b_{\chi_{eff}}^3}$	Same as I		
VI	1	Same as I	Same as I	Same as I	Same as I	6	21
	2	Same as I	Same as I	Same as I	Same as I		
	3	Same as I	Same as I	$\mathcal{N}_{-1, 1}^{\mu_{\chi_{eff}}^3, \sigma_{\chi_{eff}}^3}$	Same as I		
Default	–	BPL2P [5]	$\text{PL}_{\frac{m_2, \min, 1}{m_1}}^{\beta_q, \frac{\sigma_m}{m_1}}$	$\mathcal{N}_{-1, 1}^{\mu_{\chi_{eff}}, \sigma_{\chi_{eff}}}$	$\mathcal{N}_{0, 1}^{\mu_{\chi_p}, \sigma_{\chi_p}}$	0	0

TABLE V. Functional forms for various models. The results presented in the main text correspond to our most preferred model (I).

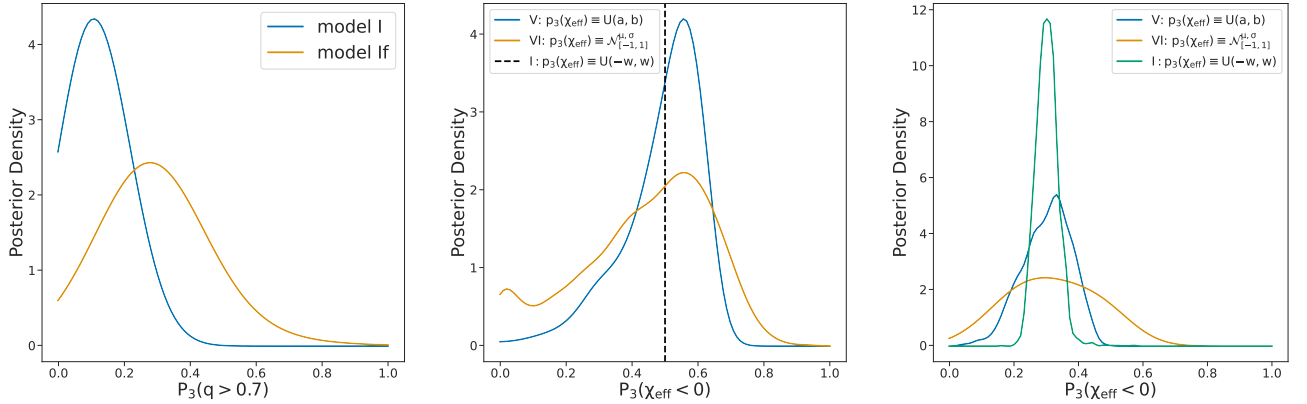


FIG. 3. Variations of the metrics $P_3(q > 0.7)$, $\sigma_{\chi_{eff}}^3$, and $P(\chi_3(eff) < 0)$ for Comp. 3 with functional forms and hyperpriors. It can be clearly seen that flexible modeling assumptions do not lead to any qualitative changes in the inferred values and only lead to a broadening of measurement uncertainties.

BBH parameters using flexible models for the joint distribution. We compare the marginal distributions of $m_1, q, \chi_{eff}, \chi_p$ with that of the default analysis as well as a data-driven inference framework based on Binned Gaussian processes (BGPs) [10, 65]. We further compare the inferred distributions of q and χ_{eff} in the mass

ranges separated by our reconstructed transition scales with the corresponding distributions yielded by the flexible BGP analysis. Since current implementations of the BGP are inherently three dimensional and unavailable for χ_p , we could not compare our inferred transitions in the χ_p distribution with data-driven analogues. Note that

Hyperparameter	Hyperprior	Prior 90%	Posterior 90%
$\alpha_{m_1}^1$	$U(-8, 4)$	(-3.49, 7.18)	(2.33, 4.28)
$m_{1,min}^1$	$U(3, 10)$	(3.00, 9.30)	(4.50, 9.12)
$m_{2,min}^1$	$U(3, m_{1,min}^1)$	(3.00, 7.13)	(3.88, 5.76)
$m_{1,max}^1$	$U(58, 100)$	(61.83, 99.85)	(62.48, 91.69)
$\lambda_{m_1}^1$	$U(0, 1)$	(0.10, 0.99)	(0.21, 0.91)
$\mu_{m_1}^1$	$U(5, 20)$	(5.78, 19.19)	(5.63, 10.69)
$\sigma_{m_1}^1$	$U(0, 10)$	(0.31, 9.24)	(0.42, 2.94)
δ_m^1	$U(0, 10)$	(0.05, 9.01)	(0.01, 8.03)
μ_q^1	$U(0.3, 0.8)$	(0.31, 0.76)	(0.31, 0.74)
σ_q^1	$\mathcal{N}_{0,\infty}^{0,0.1}$	(0.00, 0.16)	(0.00, 0.15)
$\mu_{\chi_{eff}}^1$	$U(-0.1, 0.2)$	(-0.09, 0.18)	(0.03, 0.08)
$\mu_{\chi_p}^1$	$U(0.001, 0.4)$	(0.04, 0.40)	(0.18, 0.31)
$\sigma_{\chi_{eff}}^1$	$U(0.05, 1.0)$	(0.15, 1.00)	(0.06, 0.10)
$\sigma_{\chi_p}^1$	$U(0.05, 1.0)$	(0.02, 0.29)	(0.06, 0.16)
κ_1^1	$U(-6, 8)$	(-4.68, 7.95)	(2.28, 5.91)
f_1	$U(0, 1)$	(0.00, 0.90)	(0.68, 0.91)
$m_{1,min}^2$	$\delta(m_{1,min}^1)$	-	-
$m_{2,min}^1$	$\delta(m_{2,min}^1)$	-	-
$m_{1,max}^1$	$\delta(m_{1,max}^1)$	-	-
α_{1,m_1}^2	$U(\alpha_{m_1}^1, 8)$	(-5.00, 2.68)	(-4.76, -0.63)
α_{2,m_1}^2	$U(-30, 4)$	(-3.99, 26.33)	(9.33, 27.27)
$m_{1,b}^2$	$U(30, m_{1,max}^2)$	(31.96, 49.88)	(33.61, 38.20)
β_q^2	$U(-2, 7)$	(-1.15, 6.96)	(1.65, 6.07)
$\mu_{\chi_{eff}}^2$	$U(-1, 1)$	(-0.89, 0.90)	(-0.04, 0.03)
$\mu_{\chi_p}^2$	$U(0.05, 2.0)$	(0.12, 0.97)	(0.12, 0.59)
$\sigma_{\chi_{eff}}^2$	$U(0.01, 0.2)$	(0.03, 0.20)	(0.04, 0.11)
$\sigma_{\chi_p}^2$	$U(0.05, 2.0)$	(0.07, 1.82)	(0.09, 1.25)
κ_2	$U(-6, 8)$	(-5.06, 7.47)	(-0.24, 3.20)
f_2	$U(0, 1 - f_1)$	(0.00, 0.58)	(0.07, 0.26)
α_{1,m_1}^3	$U(-4, 4)$	(-3.99, 3.20)	(-1.39, 3.63)
α_{2,m_1}^3	$U(-4, 4)$	(-3.45, 7.35)	(1.89, 6.67)
$m_{1,min}^3$	$U(m_{1,min}^1 + m_{2,min}^1, 2m_{1,min}^1)$	(6.01, 17.20)	(6.19, 17.85)
$m_{1,max}^3$	$\delta(2m_{1,max}^1)$	-	-
μ_q^3	$\delta(0.5)$	-	-
σ_q^3	$\mathcal{N}_{0,\infty}^{0,0.1}$	(0.00, 0.17)	(0.10, 0.24)
$m_{1,b}^3$	$U(30, 80)$	(31.42, 76.53)	(34.25, 74.38)
$\mu_{\chi_p}^3$	$U(0.01, 0.2)$	(0.05, 0.91)	(0.10, 0.84)
$\sigma_{\chi_p}^3$	$U(0.05, 2.0)$	(0.05, 1.79)	(0.08, 1.70)
$w_{\chi_{eff}}^3$	$U(0.01, 1.0)$	(0.03, 0.91)	(0.43, 0.62)
κ_3	$U(-6, 8)$	(-5.97, 6.60)	(1.41, 5.77)
f_3	$U(0, 1 - f_1 - f_2)$	(0.00, 0.60)	(0.01, 0.08)

TABLE VI. Hyperpriors for our most preferred model. Here $\delta(\Lambda_0)$ implies a delta function prior which fixes the corresponding hyperparameter to Λ_0 . See Table VII where we explore flexible alternatives for these restrictive hyperpriors.

our model, while being far more flexible than the default one is less so than the BGP framework, which can, in principle, reconstruct any feature in the joint distribution upto the resolution limit imposed by the choice of binning.

Both of these results are presented in Figure 8. We find the marginal distributions from our analysis and the ones recovered by the default and BGP models are consistent within uncertainties and in agreement over major features and trends in the population. Furthermore, we find the transitions in q and χ_{eff} revealed by our model are consistent with the corresponding trends recovered by the flexible BGP framework. This indicates that our

parametrizations are not leading to prior-driven conclusions regarding the astrophysical origins of BBH subpopulations.

Redshift evolution of the mass-spectrum — We now demonstrate how our results indicate a redshift evolving mass-spectrum for BBHs. As mentioned in the main text, the three components of our mixture model have distinct redshift evolution parameters. Since different components contribute dominantly to different features in the mass spectrum, our results imply that the resulting mass distribution will have distinct shapes at different redshift slices.

We first list in Table XIII, the 90% and 1σ credible

Model	Hyperparameter	New Hyperprior	Prior 90%	Posterior 90%	$\log_{10} BF$	$\log \mathcal{L}_{max}$
Ia	σ_q^1	$U(0.01, 1)$	(0.10, 0.91)	(0.14, 0.93)	6	22
Ib	$m_{1,max}^2$	$U(30, 100)$	(30.14, 94.73)	(38.32, 94.03)	6	22
Ic	$m_{1,min}^2$	$U(3, 10)$	(3.71, 9.99)	(3.55, 9.61)	6	23
Id	$m_{1,max}^2$	$U(58, 100)$	(59.90, 97.29)	(59.11, 95.61)	6	23
Ie	$m_{1,max}^3$	$U(100, 200)$	(100.71, 189.45)	(130.81, 198.66)	6	23
If	μ_q^3	$U(0.01, 1.0)$	(0.03, 0.91)	(0.11, 0.94)	6	21

TABLE VII. Flexible alternatives for certain hyperpriors used with Model I.

Hyperparameter	Hyperprior	Prior 90%	Posterior 90%
μ_m^2	$U(30, 50)$	(31.90, 49.94)	(30.53, 34.72)
σ_m^2	$U(0, 10)$	(0.89, 9.75)	(2.02, 6.28)
λ_m^2	$U(0, 1)$	(0.08, 0.98)	(0.00, 0.68)

TABLE VIII. Additional hyperpriors for model II.

Hyperparameter	Hyperprior	Prior 90%	Posterior 90%
α_m^2	$U(\alpha_m^1, 8)$	(-4.00, 2.97)	(2.02, 8.00)
α_m^3	$U(-4, 8)$	(-2.65, 8.00)	(-0.13, 3.96)
μ_m^2	$U(25, 40)$	(26.01, 39.36)	(29.67, 34.79)
μ_m^3	$U(30, 80)$	(32.25, 77.24)	(31.68, 60.68)
σ_m^2	$U(0, 10)$	(0.51, 9.49)	(2.48, 7.20)
σ_m^3	$U(5, 20)$	(6.14, 19.52)	(7.99, 20.00)
λ_m^2	$U(0, 1)$	(0.10, 0.99)	(0.29, 1.00)
λ_m^3	$U(0, 1)$	(0.06, 0.96)	(0.00, 0.74)

TABLE IX. Additional hyperpriors for model III.

intervals of κ_i for each component. It is clear that κ_2 is smaller than κ_1 and κ_3 by more than 1σ . In other words, the relative abundance of BBHs in the $35M_\odot$ feature (which are predominantly Comp. 2), decreases with redshift at the 1σ level, as seen in Figure 9.

Here we note that the $(1+z)^\kappa$ model for redshift evolution of the merger rate is inherently limited in the sense that it can often extrapolate $R(z)$ based on measurements of κ that are only informed by low redshift observations. In particular, for every mass-range, there is a maximum redshift (from here on the *detectability horizon*) above which detector sensitivity drops to zero for any finite (non-zero) ranking statistic threshold [140]. Hence, for low-mass events, the redshift evolution of the merger rate should be completely uninformed beyond the prior for high redshift values, whereas, for higher mass events, $R(z)$ can be further informed by high redshift observations. This is difficult to capture using a $(1+z)^\kappa$ which will always extrapolate $R(z)$ confidently, even for low mass subpopulations, and could likely yield incorrect results.

Hence, for correctly capturing the redshift evolution of different mass ranges, it is necessary to use flexible models for $R(z)$ such as the functional forms used in the phenomenological fits of Ref. [139], or non-parametric approaches such as those employed by Refs. [140, 141]. Furthermore, since marginal distributions are dominated by

Hyperparameter	Hyperprior	Prior 90%	Posterior 90%
μ_q^2	$U(0, 2)$	(0.21, 1.99)	(0.77, 1.03)
σ_q^2	$\mathcal{N}_{0,\infty}^{0,0.1}$	(0.00, 0.17)	(0.07, 0.21)

TABLE X. Additional hyperpriors for model IV.

Hyperparameter	Hyperprior	Prior 90%	Posterior 90%
$a_{\chi_{eff}}^3$	$U(-1, b_{\chi_{eff}}^3)$	(-1.00, 0.22)	(-0.92, -0.16)
$b_{\chi_{eff}}^3$	$U(-1, 1)$	(-0.76, 0.84)	(0.42, 0.60)

TABLE XI. Additional hyperpriors for model V.

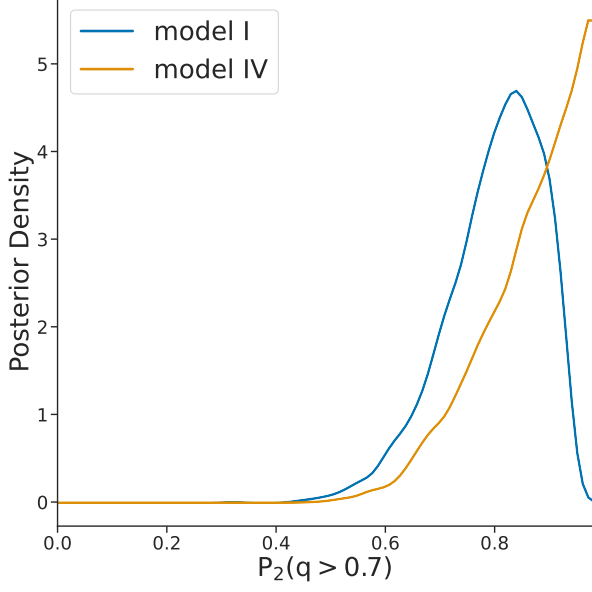
features of the subpopulation corresponding to the $10M_\odot$ peak, whose detectability horizon redshift is very small, imposing the same $R(z)$ for the entire mass-spectrum, in fact, can be problematic. In such an analysis, restrictive $((1+z)^\kappa)$ models could bias $R(z)$ at high redshifts since it will always extrapolate based on the low redshift observations in the $10M_\odot$ peak, whereas flexible models will yield uninformative $R(z)$ for high redshifts despite there being additional information in the higher mass subpopulations. In other words, modeling $R(z)$ for all BBHs independent of mass will, in general, either yield biased results or discard information present in the data. A detailed investigation of these systematics associated with inferring redshift evolution of the merger rate is ongoing.

Effective and Component Spin Populations — We now discuss the connection between properties of the effective spin distributions and those of component spin magnitudes and tilts, which is crucial to our astrophysical interpretation in the main text, particularly for the astrophysical origins of the $35M_\odot$ subpopulation. Specifically, we show how the width of the effective spin distribution increases monotonically with the preference for higher spin magnitudes, irrespective of spin orientation. We further show that for fixed magnitude values, the median of the χ_p distribution increases monotonically with the fraction of systems with in-plane spin orientations. Finally, we also show that the fraction of systems with $\chi_{eff} < 0$ is a direct measure of the ratio of aligned vs anti-aligned spin orientations with respect to the orbit.

To demonstrate these effects, we consider toy models of spin-magnitude ($a_{1,2}$) and cosine tilt ($\cos\theta_{1,2}$) distributions for various different cases. For spin magni-

Hyperparameter	Hyperprior	Prior 90%	Posterior 90%
$\mu_{\chi_{eff}}^3$	$U(-1, 1)$	(-0.83, 0.93)	(-0.36, 0.34)
$\sigma_{\chi_{eff}}^3$	$U(0, 1)$	(0.05, 0.94)	(0.09, 0.75)

TABLE XII. Additional hyperpriors for model VI.

FIG. 4. Variations of the metrics $P(q > 0.7)$ for Comp. 2 with functional forms (model I vs model IV).

tudes, we consider both fixed ($a_{1,2} \sim \delta(a_0)$) and uniform ($a_{1,2} \sim U_{0,a_{max}}$) distributions. For spin tilt angles with respect to the orbit, we explore three different cases, which are defined as follows.

1. **Preferentially Aligned:** $\cos \theta_{1,2} \sim \mathcal{N}_{-1,1}^{1,\sigma_\theta}$,
2. **Isotropic:** $\cos \theta_{1,2} \sim U(-1, 1)$,
3. and preferentially **in-plane:** $\cos \theta_{1,2} \sim \mathcal{N}_{-1,1}^{0,\sigma_\theta}$

Finally, to obtain effective spin metrics, we use all possi-

ble combinations of these magnitude and orientation distributions with three different mass-ratio distributions:

1. **Case A:** $q \sim U(0.6, 1.0)$,
2. **Case B:** $q \sim U(0.8, 1.0)$, and
3. **Case C:** $q \sim \mathcal{N}_{0,1}^{0.5,\sigma_q}$,

which are analogous to the trends we find in our inferred subpopulations. We find that all of the trends in the effective spin distributions are, overall, independent of the choice of q distributions.

We first vary a_{max}/a_0 , and, σ_θ on a grid to show, in Figure 10, that $\sigma_{\chi_{eff}}$ is a monotonic function of either a_{max} or a_0 depending on the choice of the spin magnitude

Hyperparameter	Posterior 90%	Posterior 1σ
κ_1	(2.3, 5.9)	(3.1, 5.2)
κ_2	(-0.2, 3.2)	(0.4, 2.4)
κ_3	(1.4, 5.8)	(2.6, 5.1)

TABLE XIII. Credible intervals (90% and 1σ) on the redshift evolution parameter of each component.

distribution, regardless of the distribution of spin-tilt angles. We then consider mixtures of isotropic and in-plane tilts with $\sigma_{\cos \theta} = 0.1$ and vary the mixing fraction on a grid. We show in Figure 11 that for each value of a_0 or a_{max} , $\bar{\chi}_p$ is a monotonic function of the fraction of systems drawn from the in-plane population. Finally, we show in Figure 12 that for random mixtures of aligned, isotropic, and in-plane populations, $P(\chi_{eff} < 0)$ is a monotonic function of $P(\cos \theta < 0)$.

We then compare, in Figure 13, the inferred values of $\sigma_{\chi_{eff}}$ and $\bar{\chi}_p$ for component 2 with those derived from a mixture of isotropic and preferentially inplane orientations at $\sigma_{\cos \theta} = 0.1$. We show that these metrics, while capable of constraining the fraction of excess in-plane systems, cannot yield informative conclusions on the same for component 2, given the measurement uncertainties of GWTC-4. The toy model population uses $q \sim U(0.8, 1)$ even though the exact same trends are recovered for cases A and C.

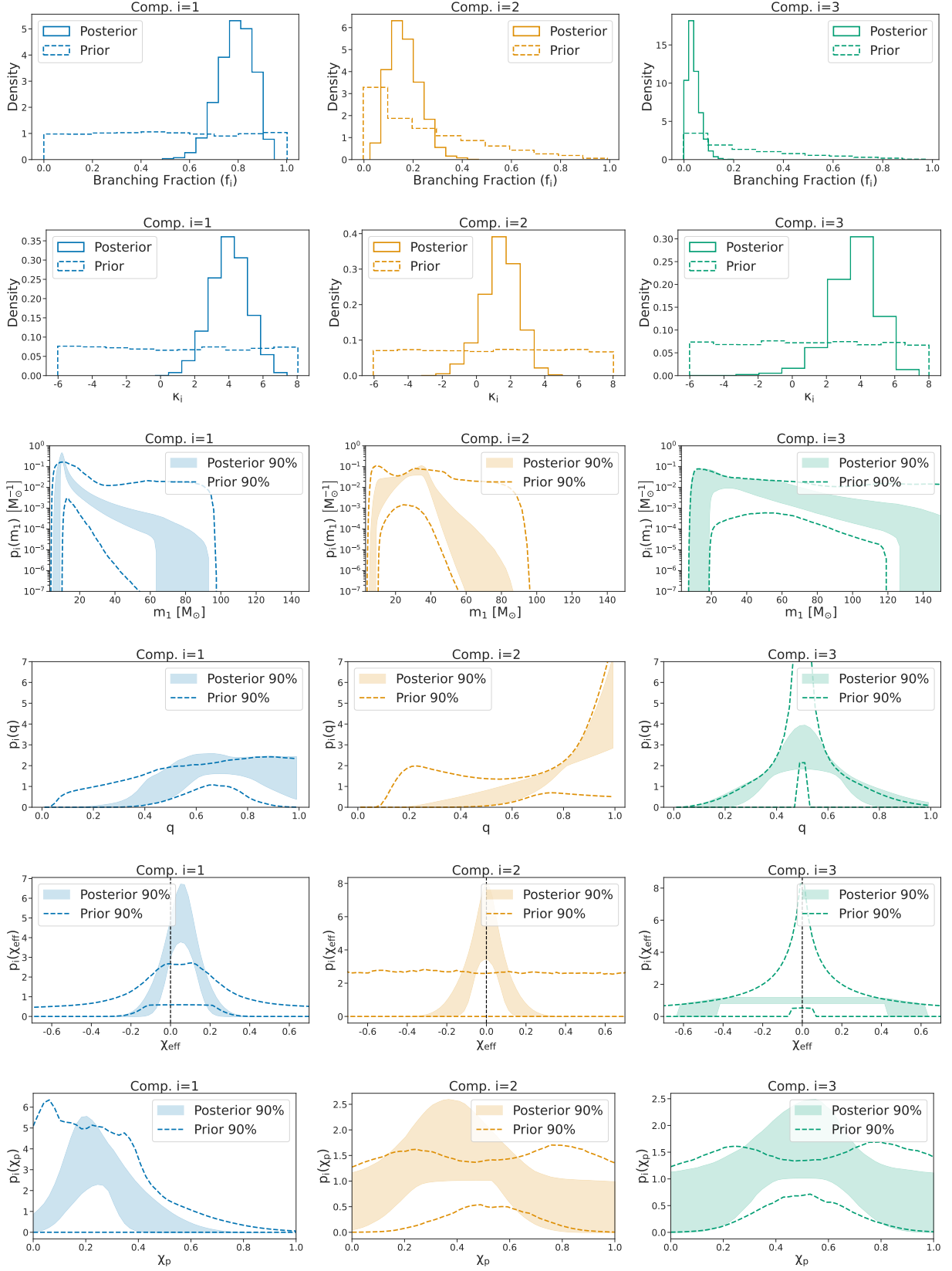


FIG. 5. Posterior vs Prior. In the top two panels, the solid lines represent the posterior density where as the dashed lines represent the prior. For the other panels, the shaded region represents the 90% credible interval of the posterior where as dashed lines enclose the 90% credible interval of the prior.

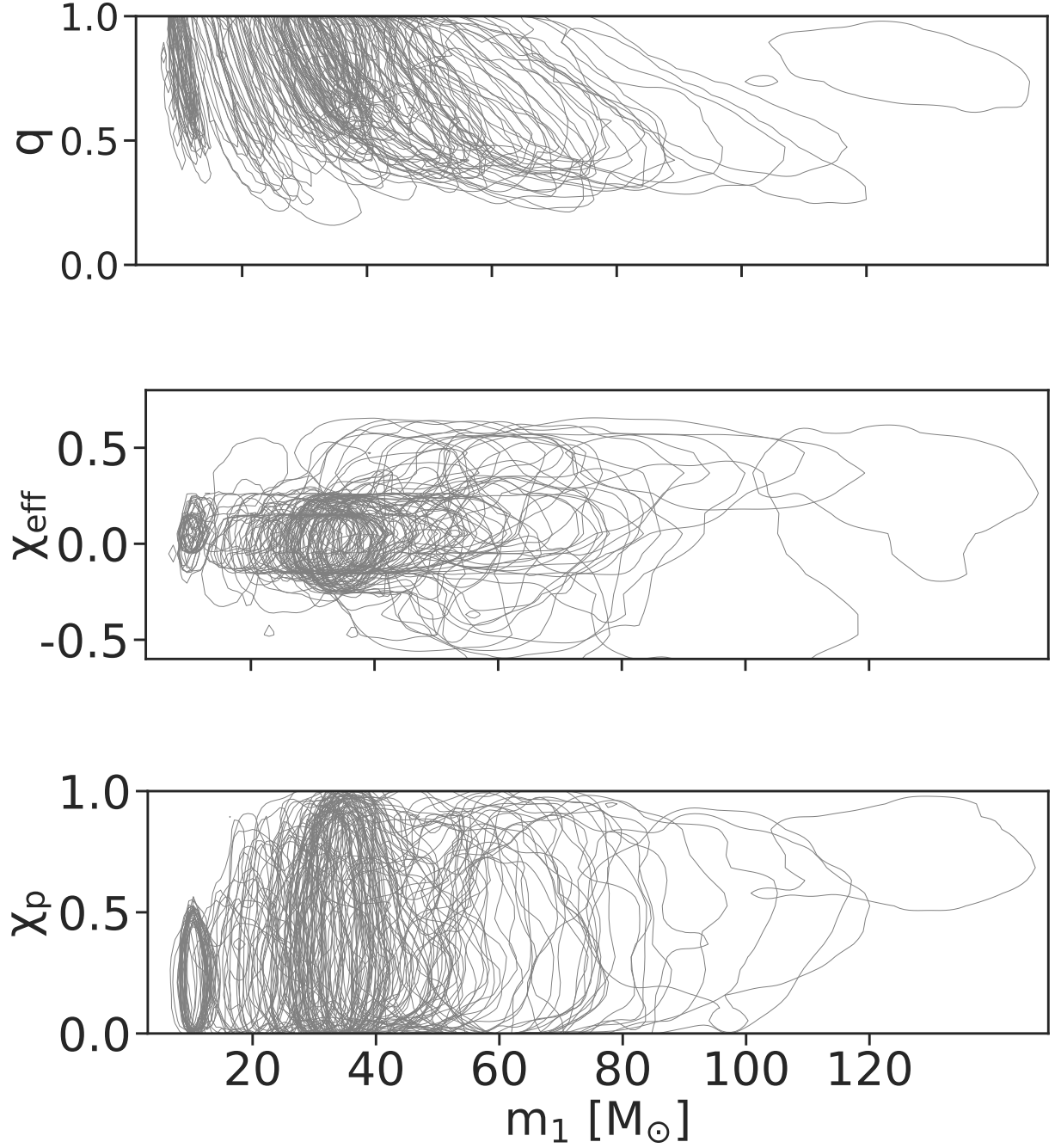


FIG. 6. Individual event measurements of the BBH parameters reweighted to the population-informed prior. Clusters of observed events that represent each of the three subpopulations and their corresponding trends can be clearly identified.

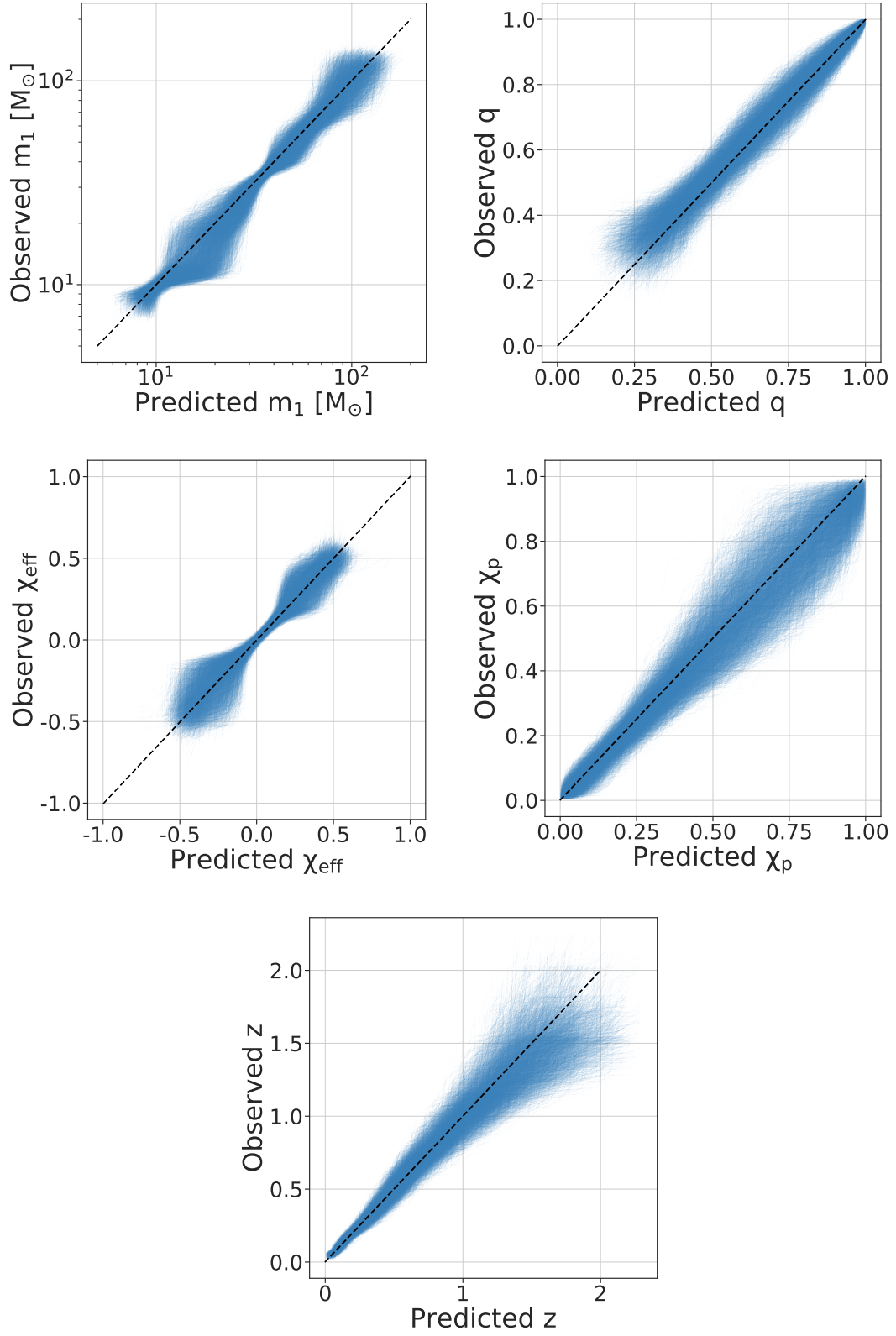


FIG. 7. Posterior predictive checks for the inferred m_1 , q , χ_{eff} , χ_p , and z distributions.

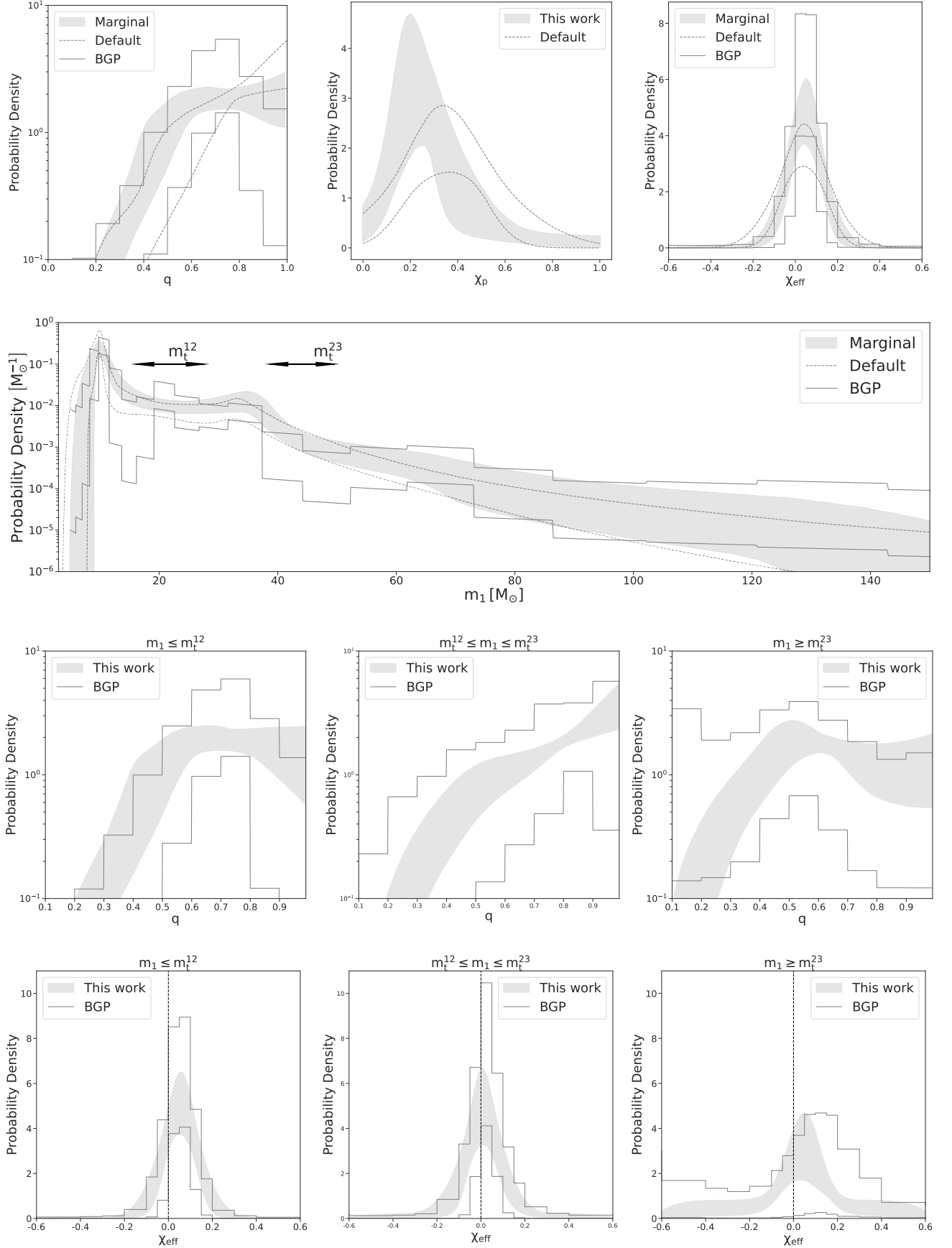


FIG. 8. Marginal Distributions of q, χ_{eff}, χ_p (first/top row) and m_1 (second row), compared with the default and BGP models. Reconstructed mass-based transitions in the q (third row) and χ_{eff} (fourth row) distributions are also compared with the corresponding BGP results.

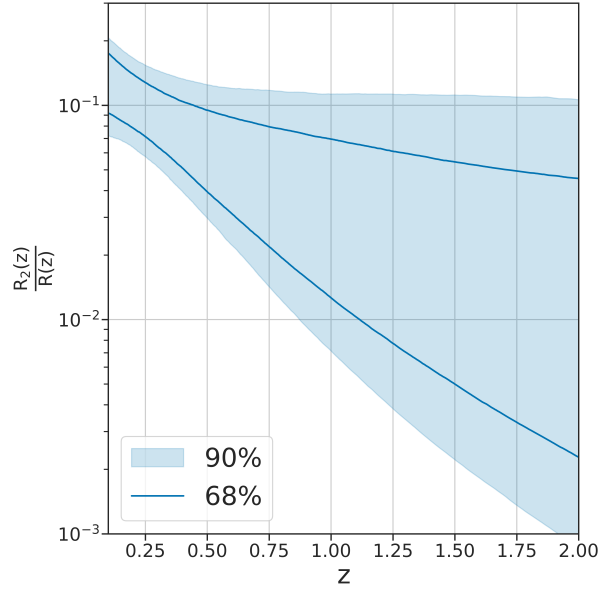


FIG. 9. The relative merger rate of Comp. 2 as a function of redshift. It can clearly be seen that the the relative abundance of Comp. 2 (which is responsible for the $35M_{\odot}$ peak) is decreasing with redshift at more than 1σ confidence.

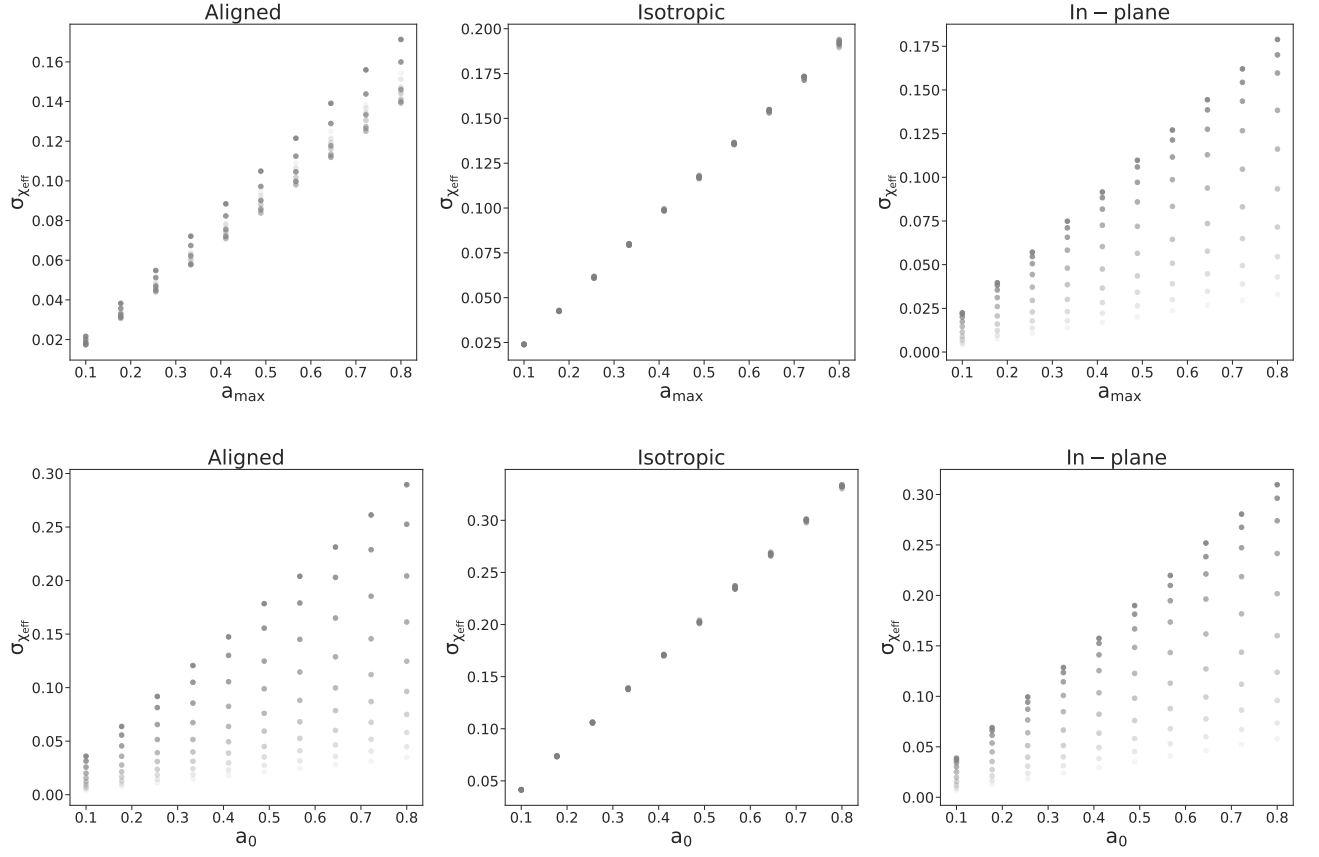


FIG. 10. The variation of $\sigma_{\chi_{eff}}$ with spin magnitude properties for the uniform (top panel) and fixed magnitude distributions. The opacity of points increases with the $\sigma_{\cos\theta}$ grid point.

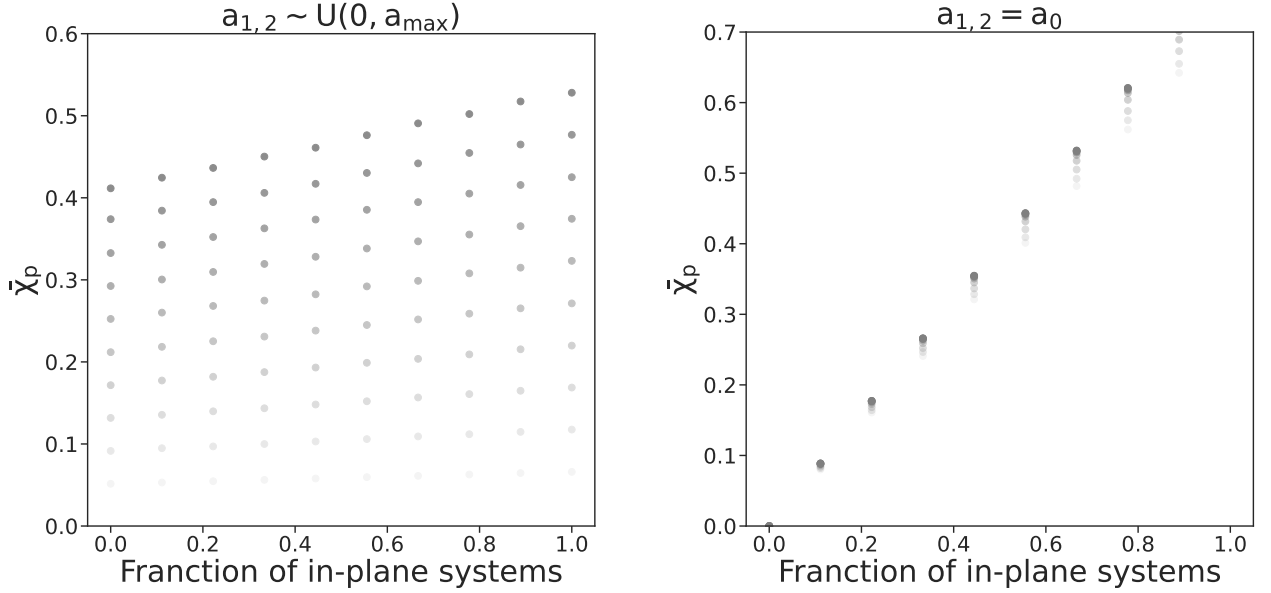


FIG. 11. The variation of $\bar{\chi}_p$ with the fraction of in-plane systems in a mixture of isotropic and in-plane populations with $\sigma_{\cos\theta} = 0.1$. The opacity of points increases with a_{max} or a_0 . We use $q \sim U(0.8, 0.1)$ for this plot even though the trends are identical for cases A and C.

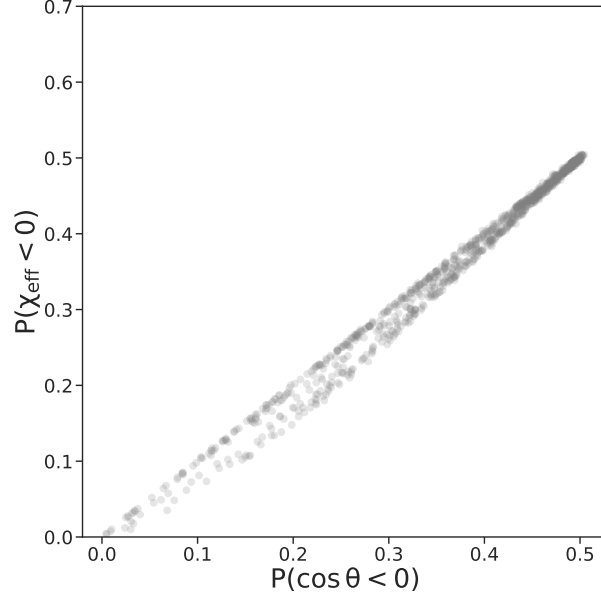


FIG. 12. The variation of $P(\chi_{eff} < 0)$ with $P(\cos \theta < 0)$ in a random mixture of **Aligned**, **Isotropic**, and **In-plane** populations. For each realization we randomly draw a value of $a_{max} \sim U(0, 0.8)$, $\sigma_{\cos \theta} \sim U(0.1, 1)$ and mixing fractions $(f_1, f_2, f_3) \sim \text{Dir}(0.33)$. Given these values we construct a mixed population of spins with f_1, f_2, f_3 being the fraction of **Aligned**, **Isotropic**, and **In-plane** systems respectively, while drawing $q \sim U(0.6, 1)$. We then compute $P(\chi_{eff} < 0)$ and $P(\cos \theta < 0)$ for each realization. We plot the resulting trend over 1000 realizations (which is found to be identical for case B and c q distributions).

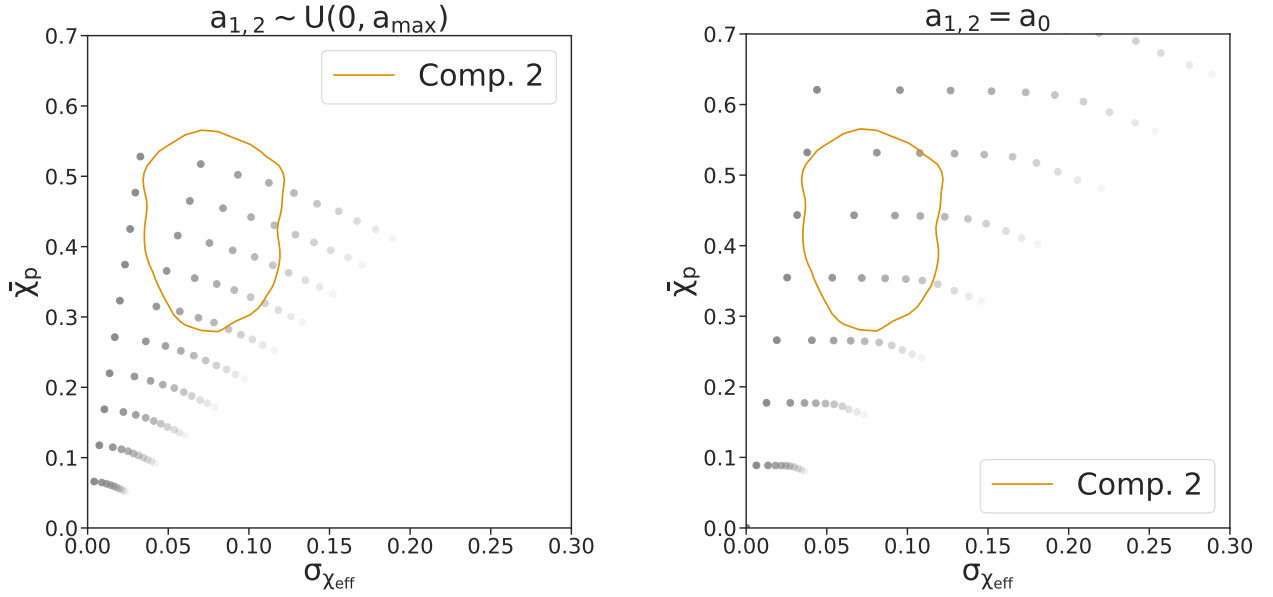


FIG. 13. The variation of $\bar{\chi}_p$ with $\sigma_{\chi_{eff}}$ for a mixture of isotropic and in-plane populations with $\sigma_{\cos \theta} = 0.1$. The opacity represents the fraction of in-plane systems and the contour represents the 90% credible interval of these effective spin metrics for component 2 as inferred from GWTC-4.